

A Review of Aeronautical Fatigue Investigations in Sweden During the Period April 2019 to March 2021



Edited by Zlatan Kapidzic
Saab AB
Sweden

Saab Doc. No. LN-060089



Submitted to the International Committee on Aeronautical Fatigue and Structural Integrity (ICAF) in conjunction to the webinar held on 30 June 2021.

CONTENT

CONTENT

- 1 INTRODUCTION**
- 2 STRUCTURAL INTEGRITY CHARACTERISTICS OF METAL MATERIALS AND STRUCTURE**
 - 2.1 Damage tolerance test verification programme for Gripen E/F airframe
 - 2.2 Fatigue testing of bolted joints with solid shims and blind fasteners
 - 2.3 Method for calculation of stress intensity factors for cracks in lugs
 - 2.4 Stress Intensity Factor (K) Solutions
 - 2.5 Continuous-time, high-cycle fatigue modelling of aluminium structure
 - 2.6 Fatigue strength of additively manufactured Ti6Al4V increased by surface post processing
- 3 FATIGUE AND DAMAGE TOLERANCE CHARACTERISTICS OF COMPOSITE MATERIAL AND COMPOSITE-Aluminium HYBRID STRUCTURE**
 - 3.1 Fatigue testing of hybrid CFRP-aluminium structure at elevated temperature
 - 3.2 Bearing strength and failure analysis of hybrid thick/thin ply composites
 - 3.3 Fatigue after impact of thin ply composites
 - 3.4 Modelling of composite bearing damage
- 4 ACKNOWLEDGEMENTS**

1 INTRODUCTION

In this paper a review is given of the work carried out in Sweden in the area of aeronautical fatigue and structural integrity during the period April 2019 to March 2021. The review includes basic studies and industrial applications.

Contributions to the present review are from the following instances:

- Saab AB
Sections 2.1, 2.2, 2.3, 2.5, 2.6, 3.1, 3.3
- Linköping University (LiU)
Sections 2.5, 2.6
- RISE SICOMP
Sections 3.2, 3.3, 3.4
- Bare AB
Section 2.4
- VTT (Technical Research Centre of Finland Ltd.)
Sections 2.1, 2.2
- OXEON AB
Sections 3.2, 3.3

2 STRUCTURAL INTEGRITY CHARACTERISTICS OF METAL MATERIALS AND STRUCTURE

2.1 Damage tolerance test verification programme for Gripen E/F airframe

Zlatan Kapidzic (Saab AB), Jan-Erik Lindbäck (Saab AB)

Background

Service life and damage tolerance capability need to be verified by testing. These tests can either be based on similarities to previously conducted tests, if applicable, or by new tests when no previous test results are available. Full-scale testing is required when:

- Changed design principles in primary load paths
- Changed material in safety-of-flight critical parts
- Significant change of stress conditions in legacy primary load paths

When Gripen A/B was initially developed, the test verification task was huge since all of the above criteria applied. Especially the implementation of the damage tolerance task according to the MIL-A-83444 specification called for test verification. An extensive fatigue and damage tolerance test program of full-scale test assemblies was accomplished, see Fig. 2.1-1. Both airframe and systems parts, e.g. actuators in the flight control system, were included and a total of about 800 artificial defects, sizing between .05 and .25 inch, were introduced in the structural parts and in the correct structural surroundings. In addition conventional full-scale static and fatigue tests of both A and B versions were conducted covering testing beyond ultimate loads and 4 lifetimes respectively.

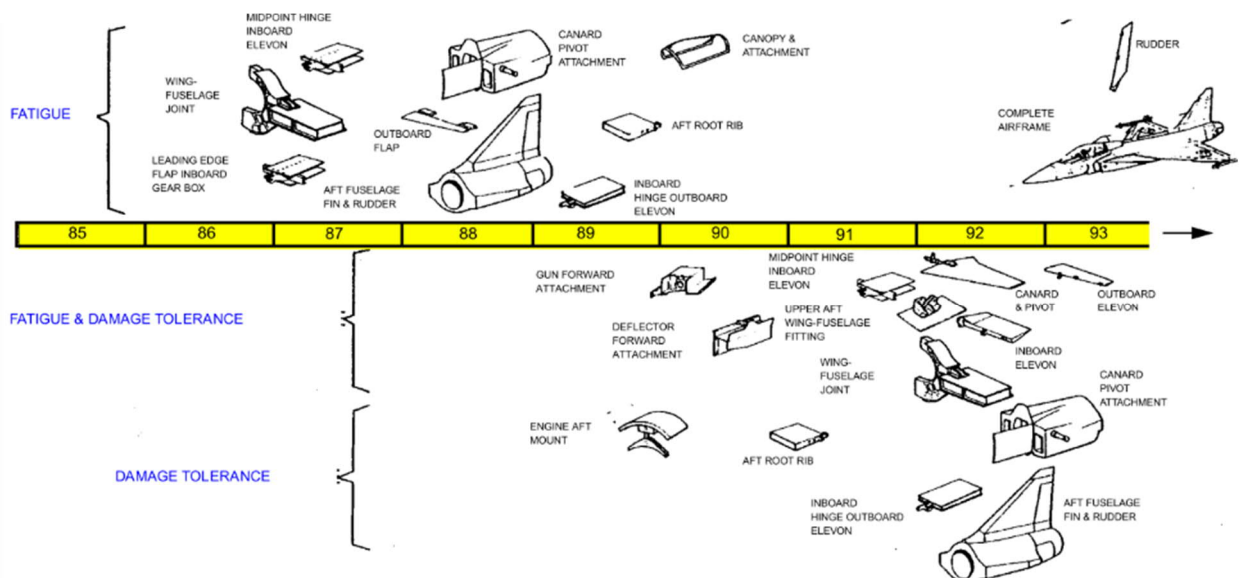


Figure 2.1-1. Test programme for fatigue and damage tolerance verification of Gripen A/B airframe.

When Gripen C/D was developed, no change of materials was done and no change of major load paths. Essential changes of local geometries were however done through the redesign to integral structures, extended service life (from 4,000 to 8,000 hours) and increased basic design mass (~10% compared to A/B versions) and some other load and structural changes, e.g. air-to-air refuelling probe, called for new full-scale fatigue tests, see Fig. 2.1-2. Damage tolerance tests were however not done in any large extent since the load path were the same although

redesigned but the validation effort done on the fracture mechanic based damage tolerance methods during the A/B developments were deemed to be sufficient also for the C/D versions.

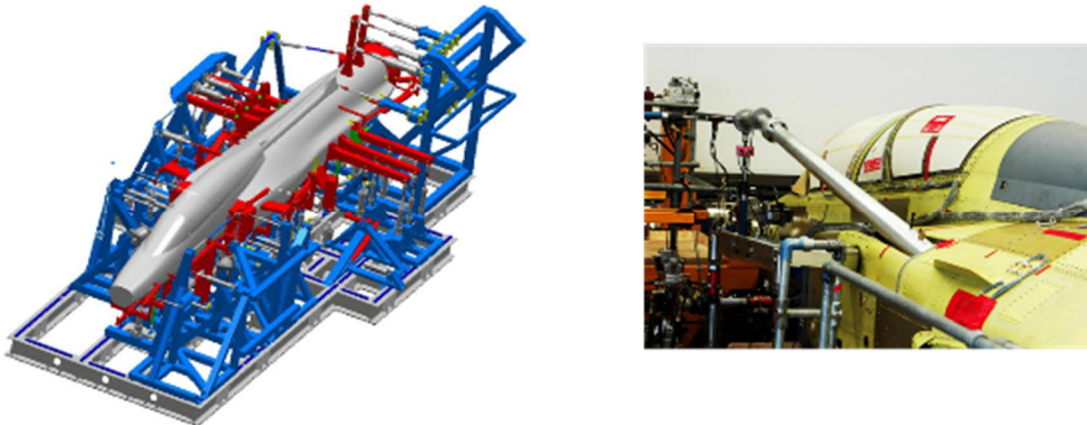


Figure 2.1-2. Full-scale fatigue test of Gripen D version.

With the development of Gripen NG versions E/F, structural changes were made that interrogated with several of the criteria for the need of test verification. Certification for airworthiness by full-scale testing is required due to:

- New mid fuselage/wing design, fuselage joints, MLG attachments
- Change of classification of parts due to design-for-manufacturing purposes
- Use of a new materials
- Increased basic design mass (~40% compared to C/D versions)
- New operational profiles

These structural changes call for a more extensive test programme than what was needed for the C/D versions. A full-scale static test (including impact damaged composite parts) of the complete airframe has been performed and two full-scale fatigue tests of the complete airframes of E and F versions are planned to be tested in the same rig for 4 lifetimes, see Fig. 2.1-3. In addition to the full-scale fatigue test, control surfaces (not included in the test airframe) will be tested in separate assemblies. These tests will be a combined fatigue and damage tolerance test by initially cycled for 2 lifetimes without artificial initial defect followed by 2 lifetimes with artificially manufactured defects installed.

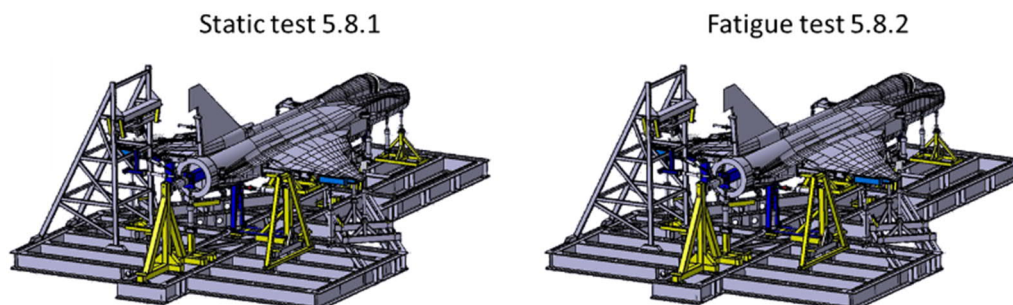


Figure 2.1-3. Full-scale fatigue tests of Gripen E version.

Full-scale tests of assemblies for compliance with damage tolerance requirements are also needed due to the structural changes in load paths and the upgraded classification of fuselage stringer joints and the design change of the wing to fuselage joint. To assure necessary and sufficient confidence regarding damage tolerance, a significant test effort designed to challenge

typical airframe crack scenarios with part through cracks (surface cracks in thickness steps, open and loaded holes etc.) was accomplished.

Figure 2.1-4 shows structural objects/assemblies which are verified for damage tolerance when having multiple artificial initial defects installed in critical sections. The full-scale static test of Gripen E airframe and some of the ongoing and completed tests of assemblages from Fig. 2.1-4 are described in more detail in the following sections.

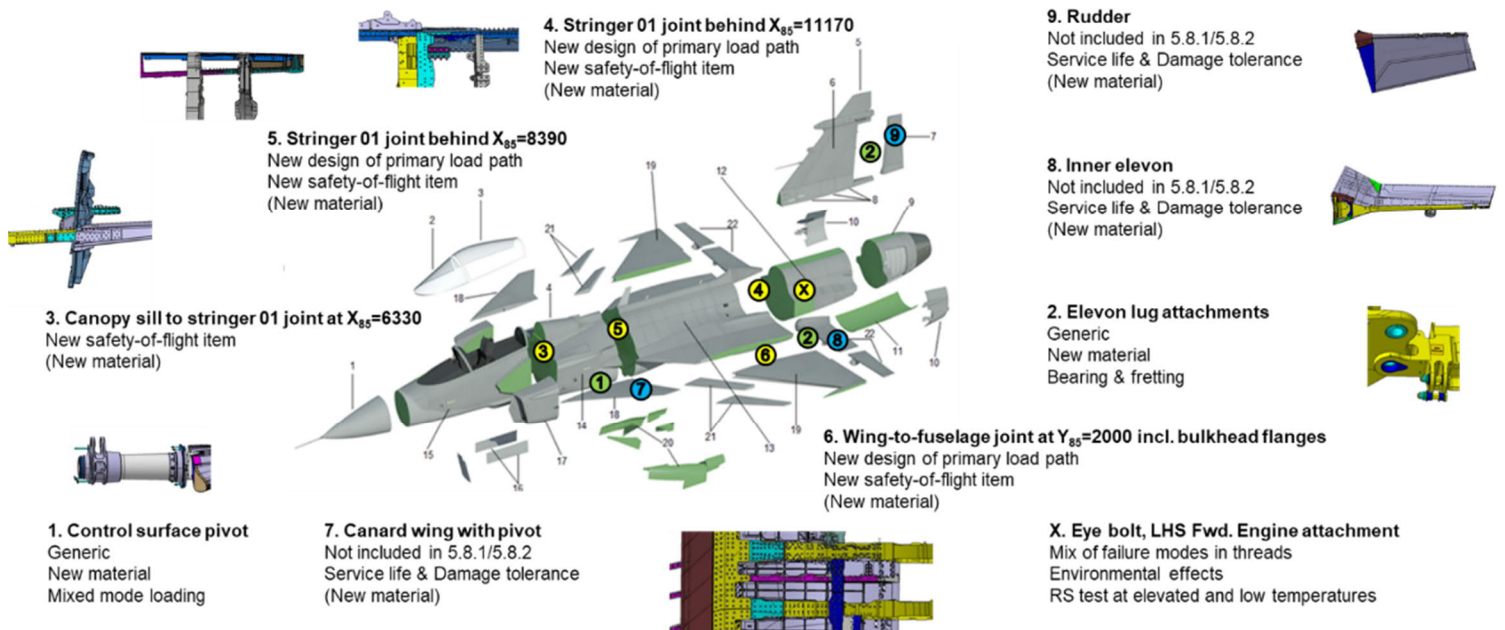


Figure 2.1-4. Full-scale damage tolerance tests of assemblies having artificial defects installed.

Full-scale static test of Gripen E airframe

A full-scale static test of the Gripen E single seater airframe has been successfully conducted. The test objectives, to verify the static strength requirements and to verify the stiffness/load distribution in the global FE-model, have been achieved. Static strength of the fuselage has been verified for 150% LL and the strength of the wing, wing joints, fin and fin attachments have been verified for 180% LL. Also the strength of the attachments for the flaps, elevons, rudder, weapon pylons, radar, AAR, landing gears, canards, air intakes and the engine have been verified by testing. This means that the test aircraft can fly without restrictions on the airframe. Only some minor outcomes in the test have led to design updates for the serial version of Gripen E.

The test object, shown in Fig. 2.1-5, consists of an airframe representing the test aircraft with fuselage, wings and fin. Landing gears, control surfaces, weapon pylons, canards and engine are replaced by “dummies” and are tested separately. The test was loaded by 126 load control channels for hydraulic actuators and 8 control channels for pressurized air in fuel tanks, cockpit and air intakes and furnished with about 2400 strain gauges for stress measurements. Impact damages were introduced at critical points in the composite skins in the wing and in the fin. Figure 2.1-6 shows the arrangement and the impactor used for introduction of horizontal impact damage on the fin.

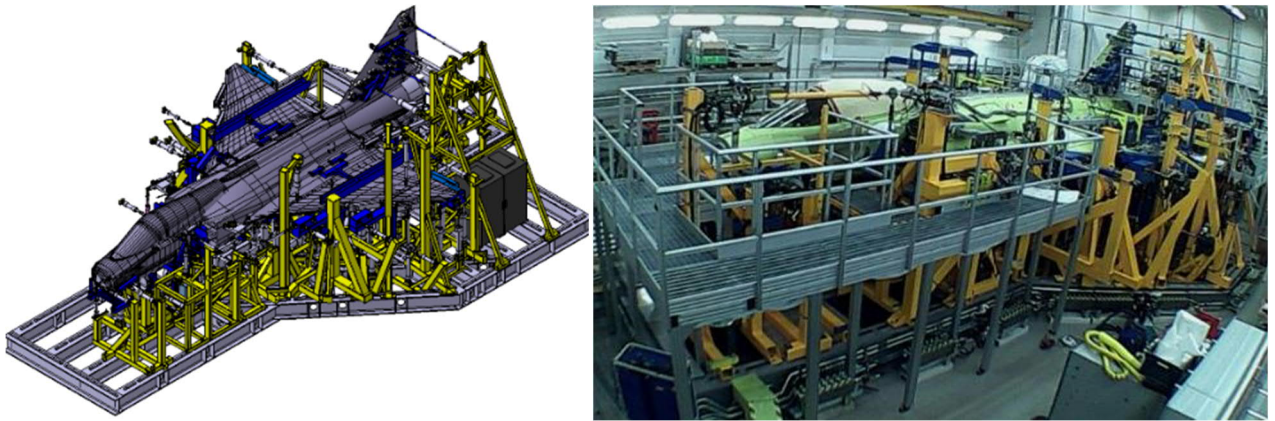


Figure 2.1-5. Static test set-up, Gripen E airframe.

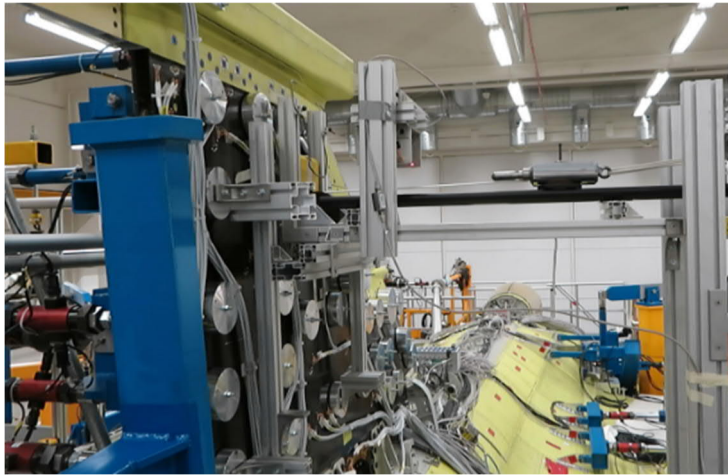


Figure 2.1-6. Introduction of impact damage on the fin.

Damage tolerance tests of assemblages of airframe components

This section describes the certifying damage tolerance tests of assemblages: wing-to-fuselage joint (#6 in Fig. 2.1-4), canopy sill-to-stringer joint (#3 in Fig. 2.1-4), stringer joint at $X_{85}=8390$ (#5 in Fig. 2.1-4) and stringer joint at $X_{85}=11770$ (#4 in Fig. 2.1-4). The common reasons for the mentioned tests are new design, upgraded criticality level and material change, see also [1]. Although the assemblages differ in geometry and loading, the testing and evaluation procedures and approaches are similar. They are all assembled by bolted joints with multiple fasteners and fastener types in different constellations.

The test objects are mounted on a wall and the loads are applied by actuators, as shown in Figs. 2.1-7 to 2.1-10. FE-models of the test setup are used to match the critical section test loads to the loads in the global FE-model of the aircraft. Refined versions of the test models are used for computation of local strains, comparison to the measured strains in the test, and computation of local stresses that are used for fatigue crack growth predictions.

In each test object 10 - 20 artificial defects were introduced by electro-spark machining and saw-cutting at critical points in the joint, mostly in fastener holes, plate radii and surface edges. The tests were first run for 2.6 DSL with 100% nominal spectrum loading where after a residual strength test was performed at 120% LL. After that, the spectrum loads were increased by a factor of 1.2 and the tests are run for an additional 1.3 DSL and another residual strength test is done at 144% LL.

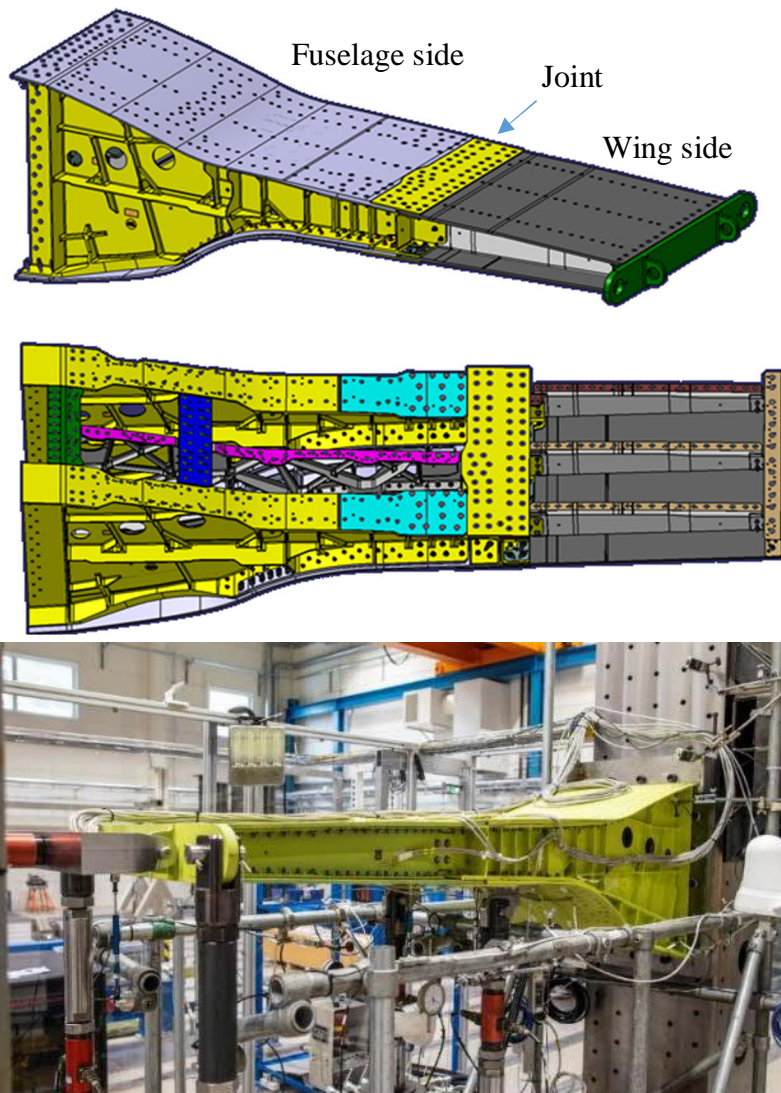


Figure 2.1-7. The test object and arrangement of the wing-to-fuselage joint test.

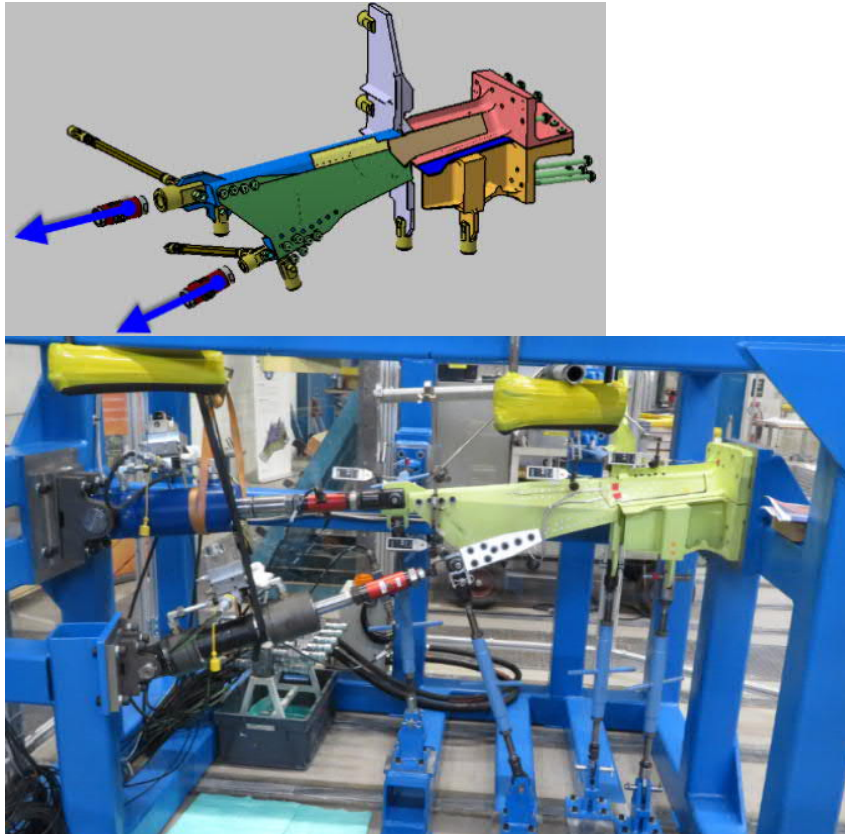


Figure 2.1-8. The test object and arrangement of the canopy sill-to-stringer joint test.

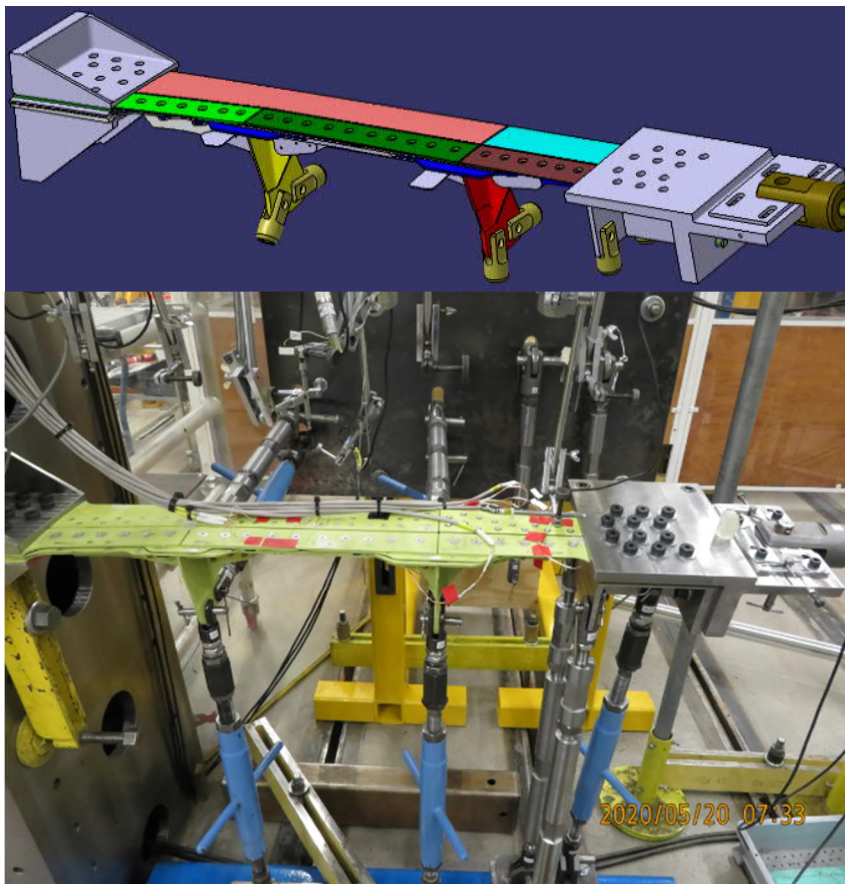


Figure 2.1-9. The test object and arrangement of the stringer joint test behind $X_{85}=8390$.

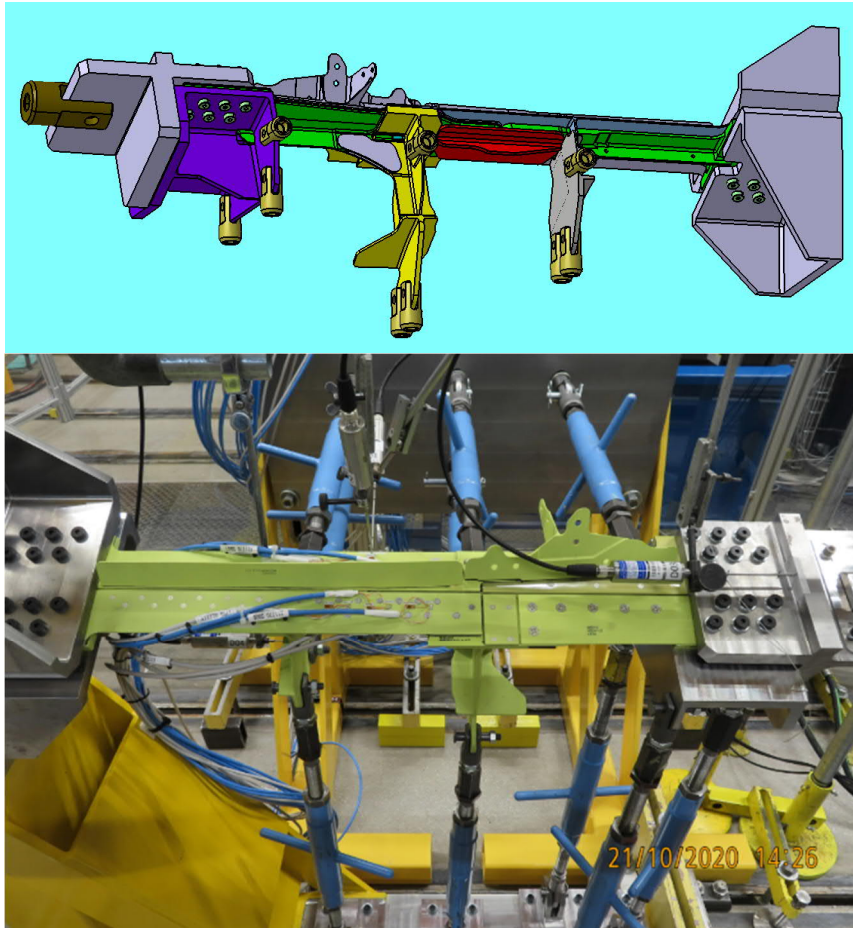


Figure 2.1-10. The test object and arrangement of the stringer joint test behind $X_{85}=11770$.

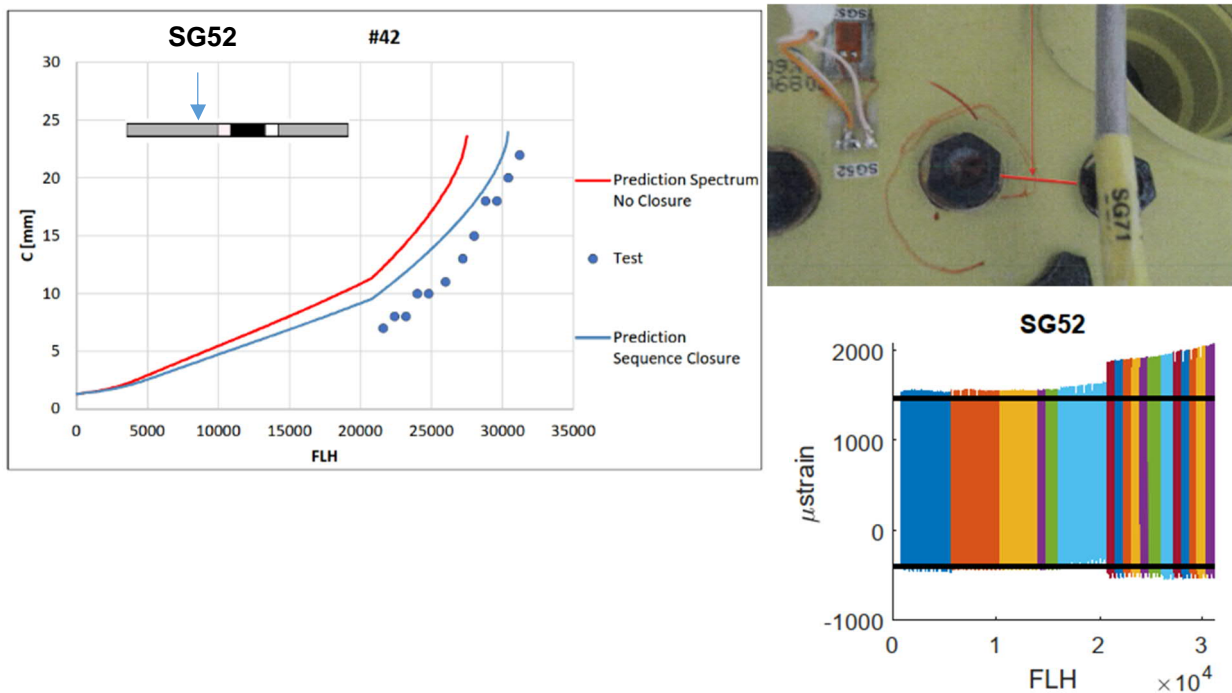


Figure 2.1-11. Crack growth prediction, max/min spectrum strain prediction (black lines) and corresponding measurements near defect #42 in a bolt hole in the joint plate of the wing-to-fuselage test.

Fatigue cracks emanated and grew to significant lengths from about half of the artificial defects. The crack growth at inspectable defects was measured during regular inspections by eddy current and the final crack lengths were measured in a tear down inspection. No unstable crack growth took place during the spectrum loading nor during the residual strength tests in any of the test objects.

Continuous strain measurements were performed during the test in the far-field areas but also in the vicinity of the defect locations. Figure 2.1-11 shows an example of the measured and predicted crack growth and strain near one of the defects in the wing-to-fuselage test. The continuous strain measurement during the tests was found to be particularly useful for evaluation and verification of predicted strains and also for monitoring of the local load levels. Figure 2.1-11 shows an increase of the tensile strain that is caused by strain redistribution due to growth of the nearby crack. The change of the strain can thus be used as an indicator of crack growth.

Rudder

Jan-Erik Lindbäck (Saab AB), Zlatan Kapidzic (Saab AB) and Risto Laakso (VTT)

This chapter highlights the international cooperation research activities between Saab Aeronautics (Sweden) and VTT (Finland).

The Rudder fatigue and damage tolerance (DT) test will be performed in 2021 performed in Finland in collaboration with VTT Technical Research Centre of Finland Ltd and its partners Eurofins Expert Services Ltd and Arecap Ltd. Figure 2.1-12 show the test set-up, which is the result from a close cooperation between the parties. Actuators will apply the air-loads to the pads on the Rudder via a simple whiffle tree. The rig contains the actuators as a floating and free-standing unit, i.e. the actuators are integrated in the rig itself. All support reactions, actuator loads and actuator displacements will be measured. There will also be a number of strain gauges and displacement transducers attached to the Rudder. At the time of writing the review, manufacturing of the rig parts is almost finished and the data acquisition system is assembled. The rudder is expected to be in the rig in late June, the test readiness review is expected in August and the project is awaited to finish in April 2022 at VTT [2].

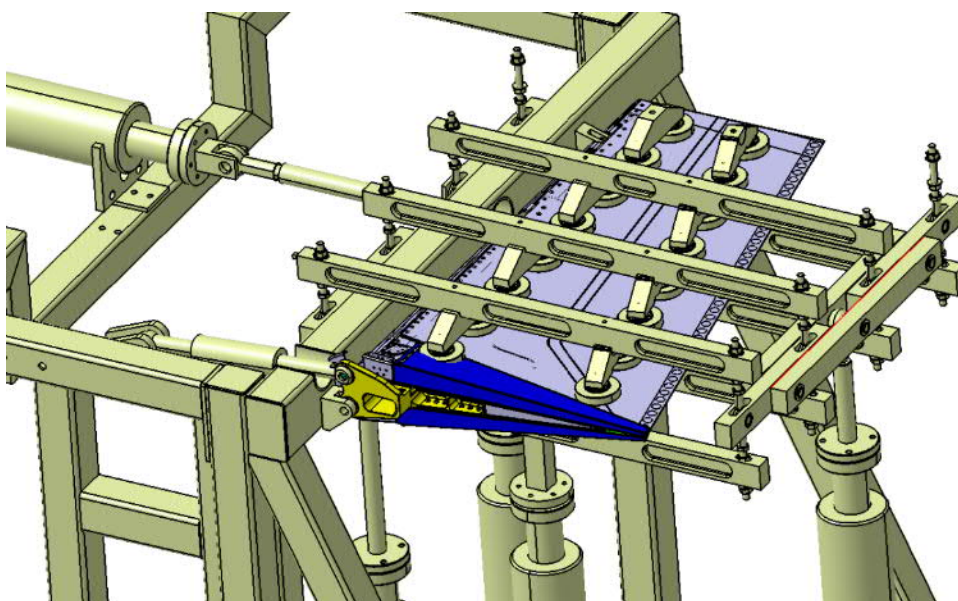


Figure 2.1-12. Rudder Fatigue and DT-test object and test rig

Spectrum loading representing two design life is applied initially as the fatigue test part. Then artificial defects are introduced at locations with the lowest strength margins in the DT-analysis and another two design life loading is applied. This is followed by a residual strength test (RST) to 120% LL (Limit Load). There is an option to increase both spectrum loads and residual strength loads another 20% after this initial test campaign and to run another design life, provided that no findings is observed after the initial DT-test. Periodic non-destructive eddy-current, ultrasonic and visual inspections will take place at critical locations throughout the test campaign. Strain gauge results will be recorded also for the sequence loading, similar to what was described in Figure 2.1-11 for the stringer joint test. The big data gauge results will be used to check for local stiffness variations in the structure that can indicate a crack initiation and/or growth.

References

- [1] Kapidzic Z. A Review of Aeronautical Fatigue Investigations in Sweden During the Period April 2017 to March 2019, ICAF 2019 Proceedings of the 36th Conference, Krakow, Poland.
- [2] Laakso R. 2021. [In preparation] Rudder Tests, Issue 1, Rev0.90. Customer Report No VTT-CR-00133-20 (classified). Espoo: VTT Technical Research Center of Finland Ltd.

2.2 Fatigue testing of bolted joints with solid shims and blind fasteners

Zlatan Kapidzic (Saab AB), Keijo Koski (VTT)

This chapter highlights the international cooperation research activities between Saab Aeronautics (Sweden) and VTT (Finland)

Introduction

A fatigue sizing method for bolted joints in AA7050-T7451 and AA2050-T84 was earlier developed at Saab based on testing of joint specimens performed at VTT, see chapter 2.8 in [1]. The method is based on results from CA testing of six different specimen geometries at different load ratios and with different amounts of secondary bending. The test data were fitted to an equation representing the Haigh diagram on which the cumulative damage calculation is based. Some spectrum tests were performed for purposes of validation and further comparisons to the results from the literature were done with satisfactory results. Since the publication of the results in [1] the method was expanded to include joints with low clamping force. Such applications may include joints with small fasteners, relatively large clamping lengths, blind fasteners, rivets or liquid shims although there is not much test data available for systematic categorization of joint fatigue life based on the clamping force.

The current study is focused on evaluating the fatigue life of joints with solid shims and Ti-screws, and joints with three types of blind fasteners B-bolt, Visu-lok and ZJQ.

Test specimens

Totally 36 single shear butt joint specimens were tested. The plate material in all specimens is AA7050-T7451 and all specimen types have two columns of countersunk fasteners but different fastener types. Six specimens of each of the following specimen types were tested in spectrum loading:

- Type D, three row specimen with 6 mm Ti-screws
- Type D-S, three row specimen with 6 mm Ti-screws and a shim plate
- Type C, two row specimen with 5 mm Ti-screws
- Type C-B, two row specimen with ~5mm B-bolts MS21140
- Type C-V, two row specimen with ~5mm Visu-lok fasteners NAS1672
- Type C-Z, two row specimen with ~4.1mm ZJQ fasteners, CR7774S Cherry Maxibolt

Specimen type D is the reference for D-S and specimen type C is the reference for C-B, C-V and C-Z. Refer to Fig. 2.2-1 where the drawing of D-S specimen type plates are shown. The drawings of the other specimen types are not shown in this report but apart from the absence of the shim plate and different number of fastener rows, they have a similar configuration as the D-S type.

The bolt holes in specimens with Ti-screws, D, D-S and C, were made with H10 tolerance according to the “Near Full Size” (NFS) procedure. No deburring or surface treatment was applied. Pretension torque was applied on the Ti-screws according to standard aerospace recommendations (6.3 Nm for M6 and 4.1 Nm for M5).

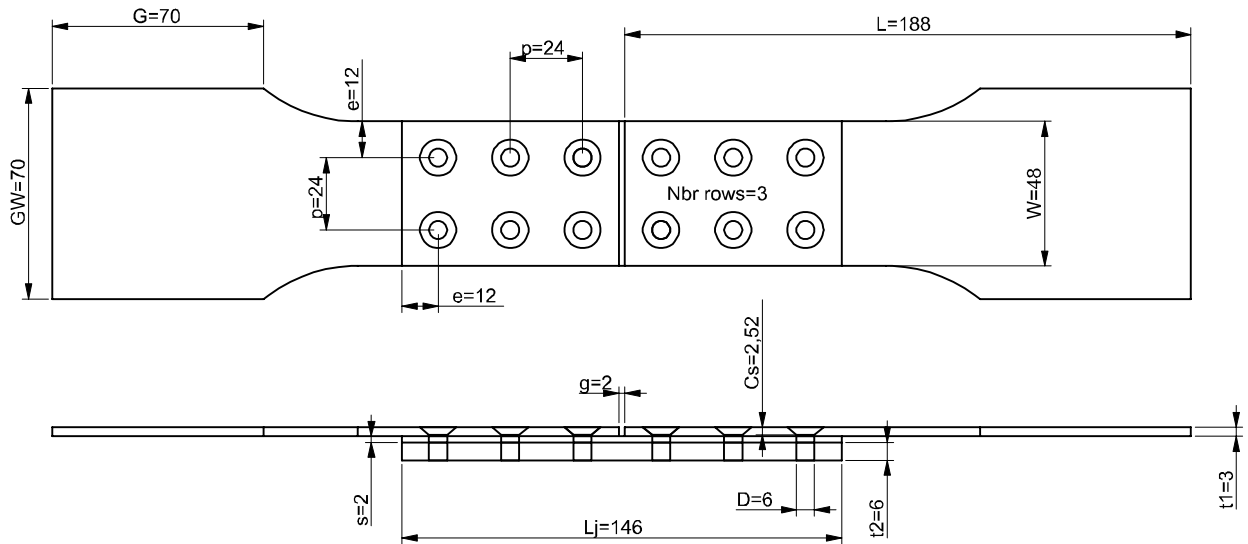


Figure 2.2-1. Drawing of specimen type D-S.

Test setup

The testing was performed at room temperature at a maximum load frequency of 10 Hz. The same tension dominated load spectrum L28E2 as in [1] is used on all specimens. It consists of ~60 cycles/flight hour. All specimen types were tested at two maximum spectrum gross stress levels, referred to as low level and high level.

The same uniaxial testing machine as in [1] was used in this test programme. The secondary bending was reduced by use of a lateral support device specifically designed for the specimens, see Fig. 2.2-2.

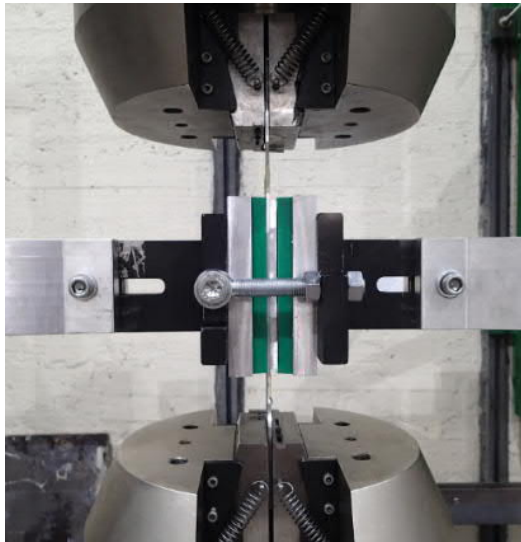


Figure 2.2-2. Test machine with lateral support.

Test results

The first three specimens that were tested, D:1, D:3 and D:4, had surprisingly low lives (~ 5000 FLH). Upon inspection, it was noted that none of the specimens of specimen types D, D-S and C had any washers installed under the nuts. In further examination of the specimens, it was observed that the nuts were torqued to the end of the bolt thread without properly clamping the

joint. The specimens were then properly reassembled with washers and the testing was continued. A significant increase of fatigue life (~5 times longer) was achieved on the reassembled D specimens and the remaining specimens were tested without any interruptions. This unintentional mistake has confirmed the importance of the clamping for the fatigue life of a joint.

All specimens failed due to fatigue in macroscopic mode I or I*, see Fig. 2.2-3 for definition of the failure modes, except specimen D-S:6 which failed in mode II.

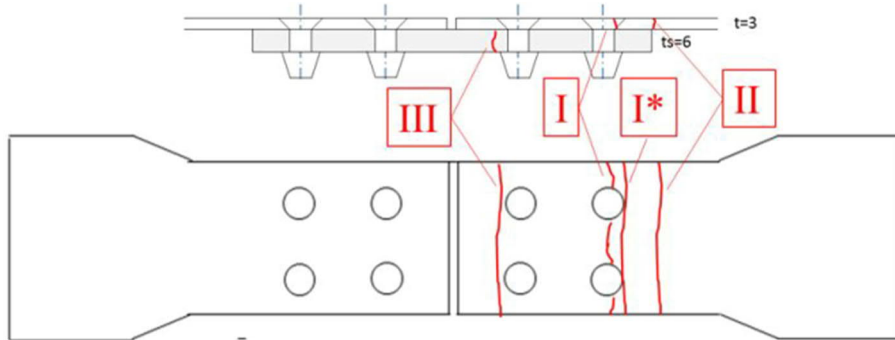


Figure 2.2-3. Failure modes.

Comparison of predictions and test results

Predictions of fatigue life of the test specimens are performed using the method in [1]. Cumulative damage is assumed equal to 1 at failure and Haigh diagrams for both normal clamping (NC) and low clamping (LC) were used in the calculations. Figure 2.2-4 shows the comparison for D and D-S specimens and Fig. 2.2-5 for C, C-B, C-V and C-Z specimens.

Comments regarding D and D-S specimens, Fig. 2.2-4:

- D specimens without washers have significantly lower fatigue lives than the specimens with washers and they tend to the LC prediction curve.
- D and D-S specimens have similar fatigue lives, which are well predicted by the NC curve. The results indicate that the shims do not influence the fatigue life of the joints.

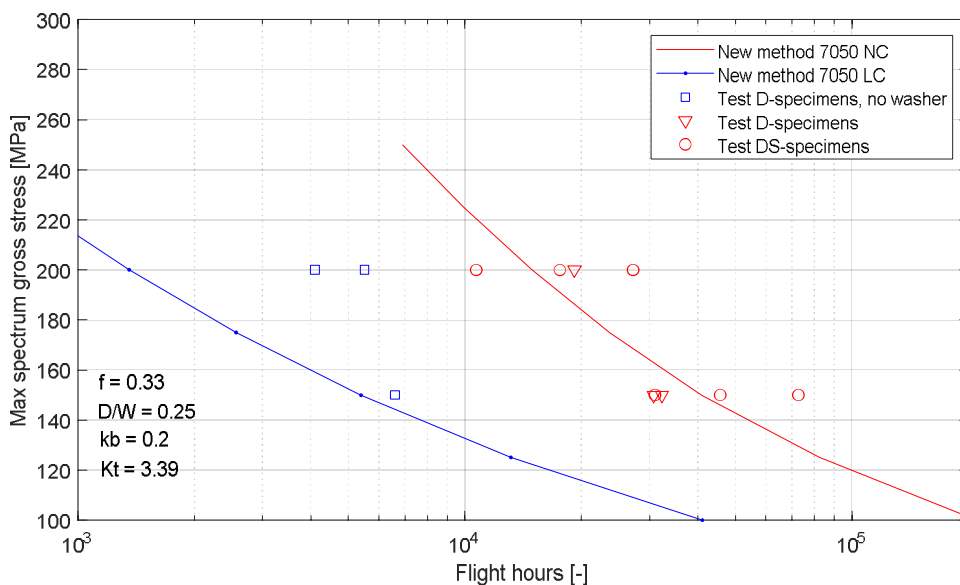


Figure 2.2-4. Test and prediction results for D and D-S specimens. NC = Normal Clamping, LC = Low Clamping.

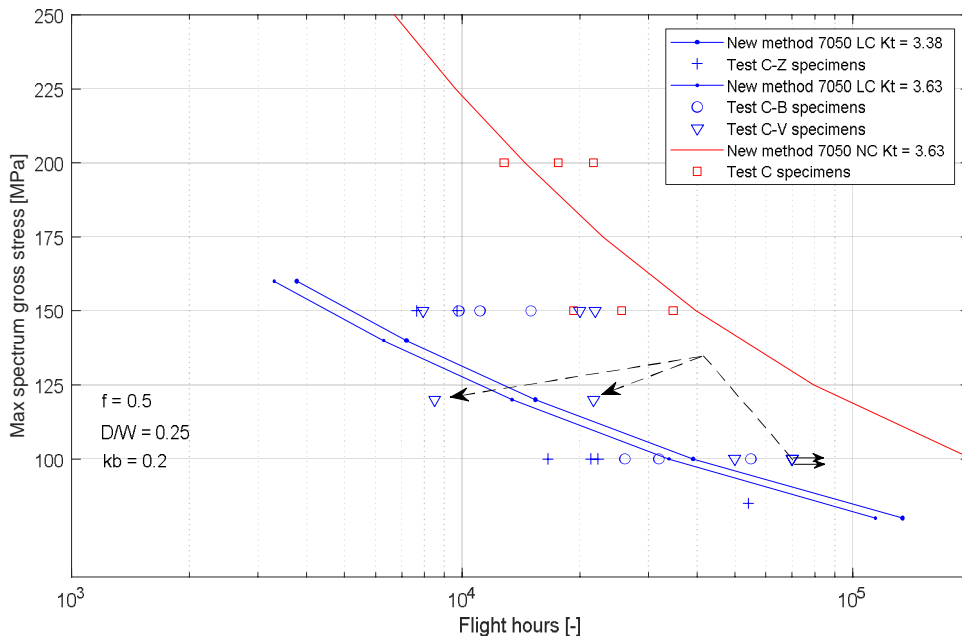


Figure 2.2-5. Test and prediction results for C, C-B, C-V and C-Z specimens. NC = Normal Clamping, LC = Low Clamping. Small arrows denote run-outs and dashed arrows denote re-runs.

Comments regarding specimens C, C-B, C-V and C-Z, Fig. 2.2-5:

- The reference specimens C have significantly longer average fatigue lives than C-B, C-V and C-Z specimens although there is a slight overlap of the data at 150 MPa stress level. Specimen type C failed mostly in mode I* while the blind fastener specimens failed only in mode I, see Figs. 2.2-6 and 2.2-7, which indicates the presence of higher clamping load in specimen type C.
- The NC prediction curve is close to the C-specimen data with an over-prediction of a maximum factor of 2, which is in the range of scatter, cf. [1].
- The LC prediction curves goes thru the C-B, C-V and C-Z data at 100 MPa but under predicts it somewhat at 150 MPa. The reason for the latter might be that the blind fastener specimens do have some clamping.
-



Figure 2.2-6. Failure mode I* in C specimen.



Figure 2.2-7. Failure mode I in C-B specimen.

References

- [1] Kapidzic, Z. A Review of Aeronautical Fatigue Investigations in Sweden During the Period April 2017 to March 2019, ICAF 2019 Proceedings of the 36th Conference, Krakow, Poland.

2.3 Method for calculation of stress intensity factors for cracks in lugs

Zlatan Kapidzic (Saab AB)

Attachment lugs are common structural elements in primary airframe structure. They can be designed into different geometrical shapes such as straight, tapered, pear shaped or corner shaped and exposed to loads in varying directions. The available stress intensity factor solutions are often restricted to certain lug geometries and load directions. For instance AFGROW [1] has a solution for straight axially loaded lug and in [2] and [3] solutions for tapered lugs are derived.

Saabs method for crack growth calculation of corner cracks in lugs, refer to chapter 2.3 in [4], is compounded from the through crack solution for the actual case and the ratio of the geometry functions for corner crack and through crack for an axially loaded straight lug. Thus the method only requires the through crack solution for the actual case. In this chapter, an in-house finite element program is presented that computes the solutions for the through crack problem for arbitrary plane lug geometries.

Description of the FE-program

The finite element program is programmed in MATLAB. The lug geometry is defined by an inner radius and a series of points that define the outer contour of the lug. Spline interpolation is used between the outer lug points. The mesh is created automatically in such way that structured mesh is obtained in an area surrounding the hole. The crack can be placed at any node point along the hole circumference and the load can be applied at any angle. Figure 2.3-1 shows the program GUI and an example of a mesh for a lug with a crack. The black dots are the points that define the outer lug geometry.

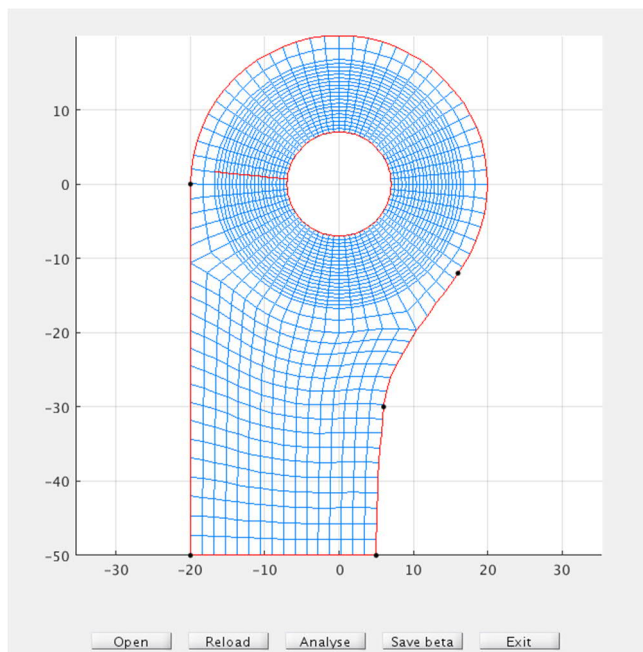


Figure 2.3-1. GUI for the FE-program.

The crack is introduced explicitly in the mesh by separation of the elements along the crack length. In the first step of the solution, the crack is forced to be completely closed using Lagrange multipliers and then the length is incrementally increased by release of the

multiplicators in the next steps. In each increment the stress intensity factors for mode I and II are computed by VCCT for both positive and negative load.

The load is applied at the middle of the mesh of bolt (not shown in Fig. 2.3-1) and the bolt-hole contact problem is solved in each increment using Lagrange multiplier technique. Besides the solutions of the geometry functions for mode I and II for positive and negative load, the program computes the normal and circumferential stresses along the hole edge and the bolt-hole gap. Figures 2.3-2 and 2.3-3 show the GUI plots with the results for the solutions with closed and opened crack respectively.

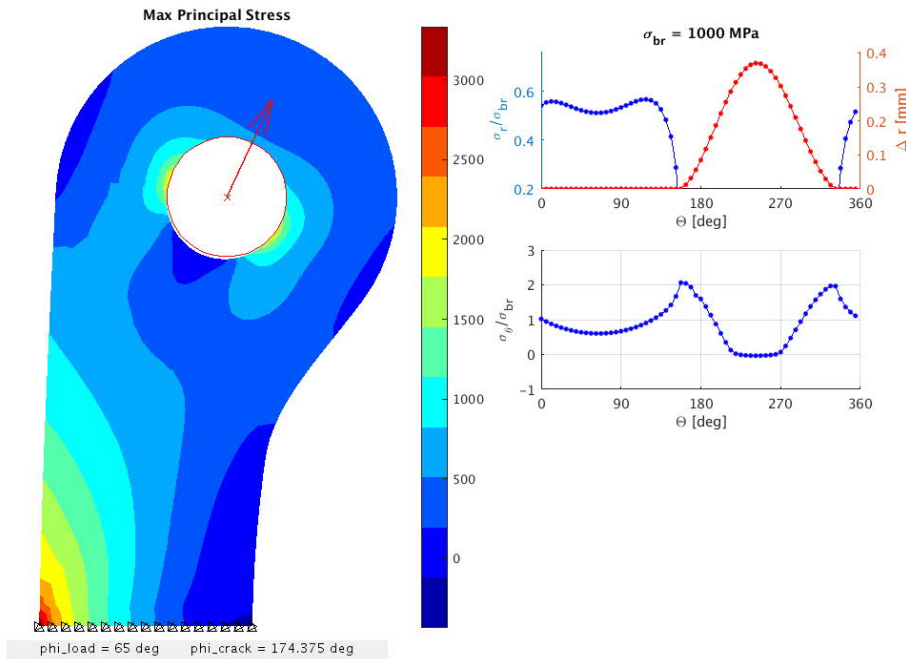


Figure 2.3-2. GUI plot of the solution with a closed crack.

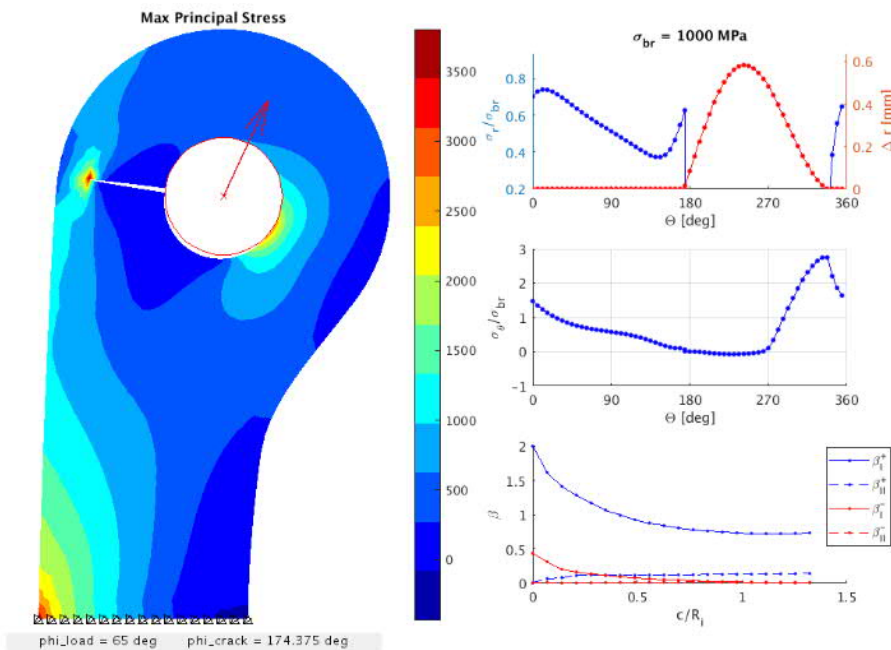


Figure 2.3-3. GUI plot for the solution with an open crack.

References

- [1] AFGROW USERS GUIDE AND TECHNICAL MANUAL. Version 5.3.5.24. 2020.
- [2] Sobotka JC, Lee Y-D, McClung RC and Cardinal JW. Stress-Intensity Factor Solutions for Tapered Lugs with Oblique Pin Loads, Proceedings of the 30th Symposium of the International Committee on Aeronautical Fatigue, June 2–7, 2019, Krakow, Poland.
- [3] Kathiresan K, Hsu TM. Advanced life analysis methods-Crack growth analysis methods for attachment lugs. AFWAL-TR-84-3080. Volume II. 1984.
- [4] Ansell H. A Review of Aeronautical Fatigue Investigations in Sweden During the Period April 2015 to March 2017, ICAF 2017 Proceedings of the 35th Conference, Nagoya, Japan.

2.4 Stress Intensity Factor (K) Solutions

Börje Andersson (BARE, AB), Jesse Vickers (Sabreliner Aviation, LLC), James M. Greer, Jr. and Gregory A. Shoales, U.S. Air Force Academy Center for Aircraft Structural Life Extension (CAStLE)

DISTRIBUTION STATEMENT A: Approved public release: distribution unlimited. PA#: USAFA-DF-2021-88

Through multiple task orders, CAStLE has sponsored the development of stress intensity factor solutions (K solutions). The prime contractor, Sabreliner Aviation, LLC, has subcontracted this effort to BARE, AB (Sweden) with Dr. Börje Andersson as the Principal Investigator. The U.S. Department of Defense High-Performance Computing (DoD-HPC) network has been a key and necessary component to the generation of these solutions.

The K solutions are suitable for implementation into crack growth prediction codes, such as AFGROW and NASGRO®. Significant theoretical development work was done to develop a valid countersunk hole loading model [1]. The focus of recent work (in priority order) has been

1. Single and double non-symmetric cracks at a countersunk hole: finish solutions for $b/t = 0.5$ where b is the length of the straight shank portion of the hole.
2. Single and double non-symmetric cracks at a countersunk hole for $b/t = 0.05$.
3. Single and double non-symmetric cracks at a countersunk hole for $b/t = 0.25$.
4. Surface “thumbnail” semi-elliptical crack (Figure 1 below)

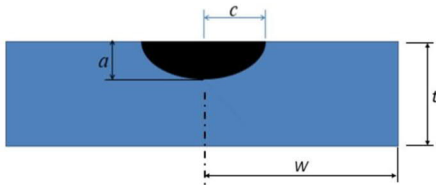


Figure 2.4-1. Surface crack in a plate subject to tension and bending.

Figure 2.4-2 defines the basic parameters considered ($D=2R$).

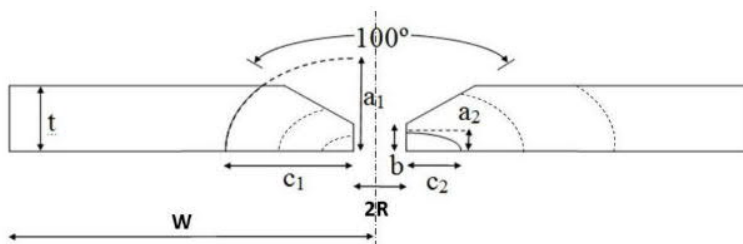


Figure 2.4-2. Crack parameters ($a_1, a_2, c_1, c_2, R, B, t, W$).

The parameter space for priorities 1–3 (above) is

$c/a = 0.10, 0.1667, 0.333, 0.5000, 0.667, 0.75, 0.800, 0.900, 1.000, 1.111, 1.25, 1.333, 1.500, 2.00, 3.000, 4.00, 5.00, 6.00, 8.00, 10.00$

$a/t = 0.10, 0.20, 0.30, 0.40, 0.50, 0.60, 0.70, 0.80, 0.90, 0.95, 1.05, 1.1, 1.20, 1.35, 1.60, 1.90, 2.40, 3.20, 4.50, 6.50, 9.00, 12.00, 15.00$

$b/t = 0.05, 0.25, 0.50, 0.75$

$R/t = 0.2, 0.333, 0.5, 0.667, 1.0, 1.5, 2.0, 3.0$ and 5.0

$W/D = 1.2, 1.3, 1.4, 1.6, 1.8, 2.0, 2.3, 2.6, 2.9, 3.2, 3.5, 4.0, 4.5, 5.0, 6.0, 8.0, 10.0, 15.0, 20.0, 50.0, 100.0$

$h/W = 1.0, 1.5, 2.0, 3.0$

As can be inferred from the large parameter space, a set of K solutions typically involves several 100 million of solutions. A complex system for checking that each solution has negligible errors have been used. A plot of typical K solution output is shown in Figure 2.4-3. Loading is simple tension for the data shown. The variable ϕ is the parametric angle locating a point along the crack front, with $\phi = 0^\circ$ being the “c” vertex. Note that when $a/t > b/t$ for a countersunk hole, the crack front ends prior to $\phi = 90^\circ$ (see Figure 2.4-2). Dependent on the angle at which the crack front intersects with the surface, K becomes zero or infinite at the vertices.

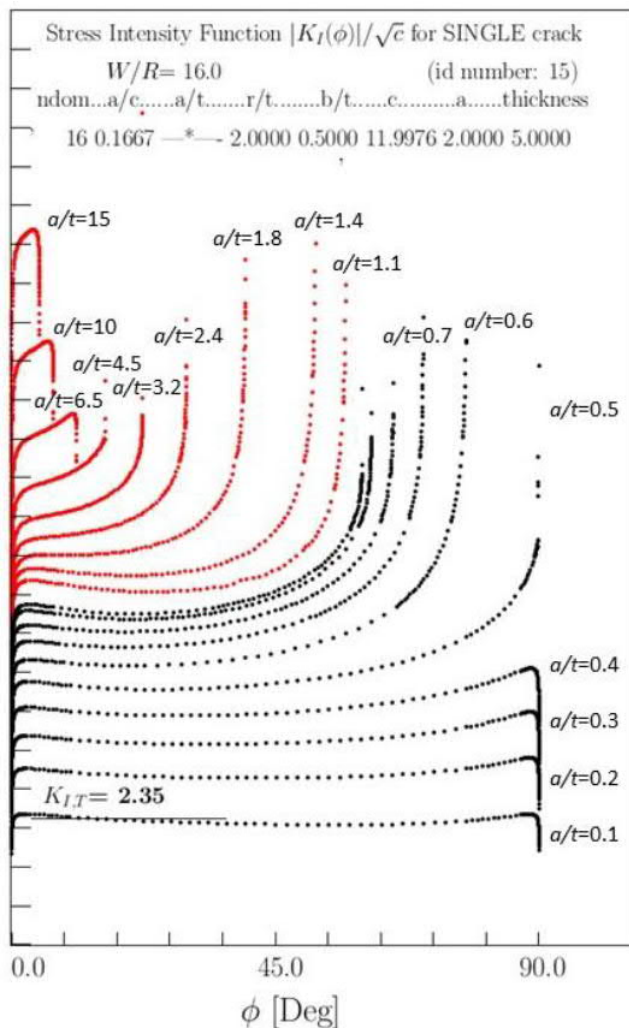


Figure 2.4-3. $K(f)$ data as a function of a/t for a fixed crack size, $c/a = 6$.

References

- [1] Andersson B. A Pin-Load Model for Worst-Case Scenario $K_I(\phi)$ Analysis, Proceedings of the 2020 AFGROW User Workshop, 14–15 September 2020, Layton, UT. <https://afgrow.net/workshop/workshop2020.aspx>, last accessed 3/17/2021.

2.5 Continuous-time, high-cycle fatigue modelling of aluminium structure

Zlatan Kapidzic (Saab AB), Stefan Lindström (LiU)

Airframe development is moving towards greater use of integrated structural metallic parts. The reasons for this are simplified assembling processes and reduction of number of articles. Figure 2.5-1 shows an example of traditionally built structure in Gripen A and a later version of the structure that has been integrated. As ever higher demands are placed on the efficiency and utilization of integrated structures the demands for ability to assess the fatigue life increase. Also, integrated structures usually have greater geometric complexity, see an example from Gripen E in Fig. 2.5-2, which is difficult to replace or repair. It is thus important that the fatigue analysis methods are adapted and capable of producing reliable results that will ensure good designs against fatigue problems.

Traditionally used fatigue sizing methods are verified and have resulted in designs with very few fatigue problems. But they are often based on simplifying assumptions like uniaxial, proportional stress with a clearly defined stress concentration factor and cycle counting methods. Given the complexity of integrated structures, there is a risk of oversimplification that may induce non-conservatism or over-dimensioning. Thus, there is a need for more sophisticated and accurate analysis methods that can include the geometric and load complexity.

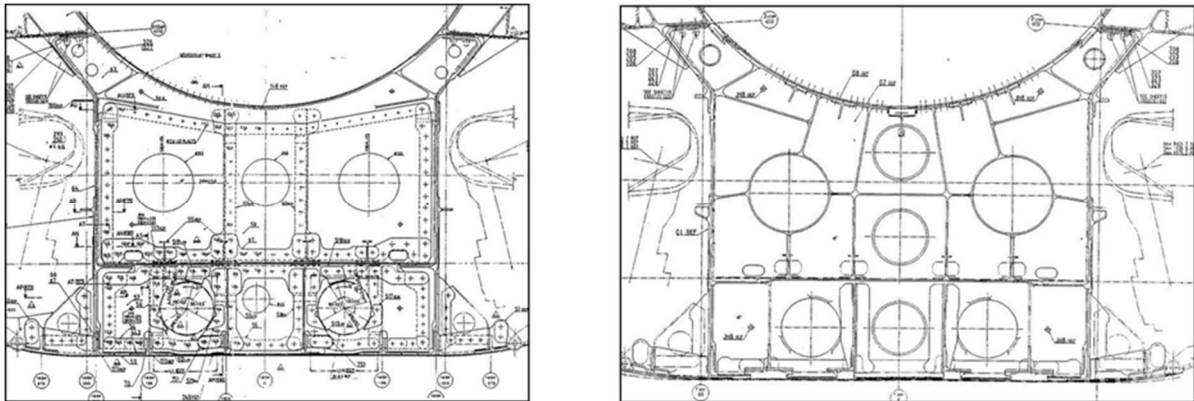


Figure 2.5-1. Built (left) and integrated structure (right).

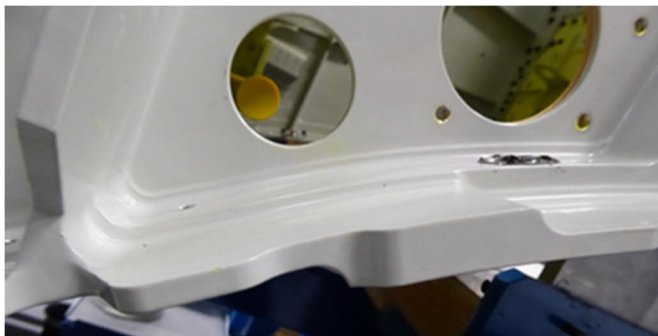


Figure 2.5-2. Detail of airframe structure.

Saab and Linköping University have therefore engaged in a project with a goal to develop a fatigue model that can take into account the complexities related to integral aluminium structure. The model is a continuation of work in [1] and is based on integration of continuous-time load histories and a concept of moving endurance surface in the stress space. The endurance surface is taken to be of Drucker-Prager type and is defined so that the function

$$\beta = \frac{1}{S_e} (\sigma_{eff} + AI_1 - S_e)$$

is equal to zero, where $I_1 = \text{tr}(\boldsymbol{\sigma})$, S_e is the fatigue limit, A is a material parameter and the effective stress is

$$\sigma_{eff} = \sqrt{\frac{3}{2}} \|\mathbf{s} - \boldsymbol{\alpha}\|$$

and where s is the stress deviator and $\boldsymbol{\alpha}$ is the backstress. The backstress is the quantity that allows for the movement of the endurance surface. The load history dependent accumulation is measured with a damage parameter D that is initially equal to 0 and equal to 1 at fatigue failure. The evolution of the damage parameter and of the backstress are defined by the following rate equations

$$\begin{aligned} \dot{D} &= \dot{\beta} g(\beta) \\ \dot{\boldsymbol{\alpha}} &= \dot{\beta} C(\mathbf{s} - \boldsymbol{\alpha}) \end{aligned}$$

which are both non-zero only if $\beta \geq 0$ and $\dot{\beta} > 0$. In other words, the damage is developing and the endurance surface is moving only if the stress state is outside of the surface and moving away from it. In the above equations C is a material parameter and $g(\beta)$ is a function that is positive if $\beta \geq 0$. Figure 2.5-3 shows an example of calculated damage development during a variable amplitude load history in [1].

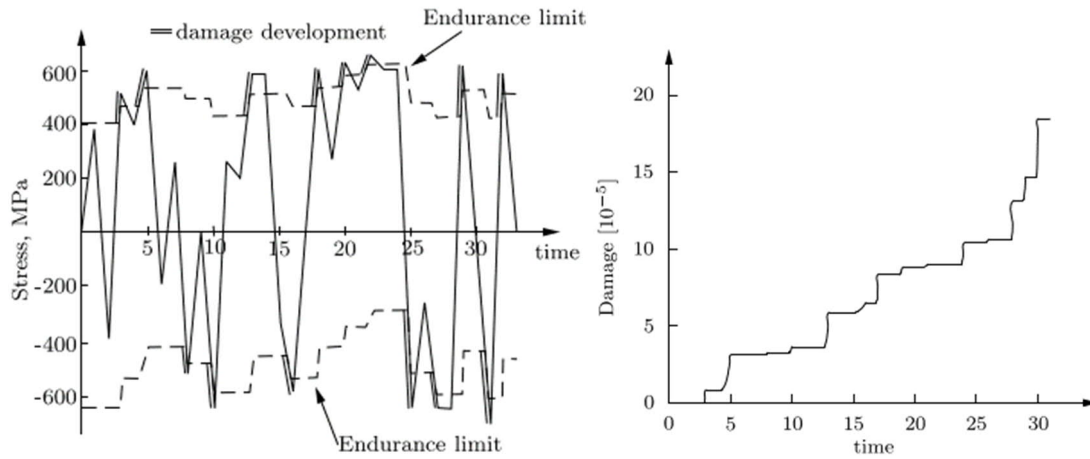


Figure 2.5-3. Example of complex load history and damage development, obtained from [1].

The set of above equation is integrated over the load history and is thus not using any cycle counting algorithm at all. It also takes into account multi-axial and non-proportional stress states. The validity range and the calibration procedure is demonstrated in [2]. Calibration of material parameters for some aluminium materials is done in [3], as well as predictions for non-proportional, biaxial stress histories and introduction of other types of endurance surfaces. Experimental and theoretical work to include effects of stress concentrations and stress gradients is currently being conducted by Saab and Linköping University and will be published during 2021 [4]. Future plans are to implement the model in finite element based codes where analyses of large integrated structures can be performed.

The work was supported by the Swedish National Aeronautical Research Program 7 of Vinnova as grant agreement No. 2019-02778.

References

- [1] Ottosen NS, Stenström R, and Ristinmaa M. Continuum approach to high-cycle fatigue modeling. *Int. J. Fatigue*, 30(6):996–1006, 2008.
- [2] Lindström SB, Thore C-J, Suresh S, Klarbring A. Continuous-time, high-cycle fatigue model: Validity range and computational acceleration for cyclic stress. *Int. J. Fatigue*, 136 (2020) 105582.
- [3] Lindström S. Continuous-time, high-cycle fatigue model for nonproportional stress with validation for 7075-T6 aluminum alloy. *Int. J. Fatigue*, 140 (2020) 105839.
- [4] Lindström SB, Moverare J, Leidermark D, Ansell H, Kapidzic Z. Incremental fatigue modeling of 7050-T7 aluminum alloy at stress-raisers, *to be submitted*.

2.6 Fatigue strength of additively manufactured Ti6Al4V increased by surface post processing

Magnus Kahlin (Saab AB), Hans Ansell (Saab AB), Johan Moverare (LiU)

Background

Additive Manufacturing (AM) for metals includes a group of production methods that use a layer-by-layer approach to directly manufacture final parts. AM offers a greater design freedom, compared to conventional production methods, which allows for parts with new innovative design. This is very attractive to the aerospace industry, in which parts could be designed to have reduced weight and improved performance contributing to reduced fuel consumption, increased payload and extended flight range. There are, however, challenges yet to solve before the potential of AM could be fully utilized in aerospace applications. One of the major challenges is how to deal with the poor fatigue behaviour of AM material that is attributed to the rough as-built surface which acts as a stress concentration and promote fatigue crack initiation. The surface can, of course, be machined, but the part design would then be restricted to conventional machining geometries and the freedom of design would be lost. In this study, several surface post processing methods that can handle different degree of complex geometries have been investigated in order to improve the fatigue strength by either reducing the surface roughness and/or introducing compressive residual stresses at the surface. The work presented below is based on two open-source scientific journal papers [1], [2] and further details on test methods and results can be found there.

Fatigue investigation

Additively manufactured Ti6Al4V manufactured with electron beam powder bed fusion (E-PBF) and laser powder bed fusion (L-PBF) have subjected to five different surface post processes:

- Centrifugal finishing, in which the part is rotated in barrel together with abrasive media.
- Shot peening, in which the part is bombarded with steel shots in order to introduce compressive stresses.
- Laser shock peening, in which a pulsed laser evaporates a thin water layer on the part and the shock wave introduces residual stresses.
- Linishing, in which a robot is controlling rotating brushes with a constant force in order to polish the surface.
- Laser polishing, the surface, 50-200 μm , is remelted by a laser in order to smoothen the surface.

Test specimens with geometries according to Fig. 2.6-1 were manufactured with final shape directly from AM and then further post processed with one of the post processes presented above. The post process parameters were developed by an iterative process with surface roughness measurements and simulations in order to obtain optimal parameters. The final parameter setup was then evaluated by fatigue testing. Constant amplitude fatigue testing was performed at room temperature using load control and stress ratio $R=0.1$. The surface roughness was determined by focus variation microscopy and the 3D-mapped surfaces and the surface roughness, R_v (maximum valley depth) are presented in Fig. 2.6-2 and Fig. 2.6-3.

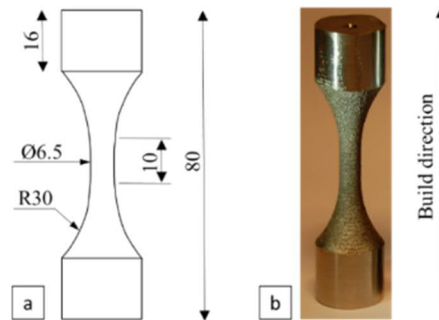


Figure 2.6-1. a.) Test specimen geometry before post processing, b.) Test specimen with as-built surface. Image from [1] with courtesy of Elsevier.

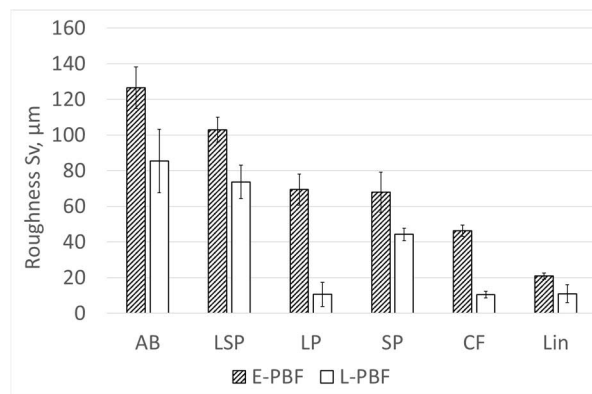


Figure 2.6-2. Surface roughness of as-built (AB) and post processed material. AB=as-built, CF=centrifugal finishing, LSP=laser shock peening, SP=shot peening, Lin=linishing, LP=laser polishing,. Image from [1] with courtesy of Elsevier.

One can see that a considerable improvement in surface roughness can be achieved but that the inherent rougher surface of E-PBF still remains also after surface processes which indicates that the deepest valleys are difficult to remove. The effect of this can be seen in the fatigue limit presented in Fig. 2.6-5 in which the post processed E-PBF cannot reach the levels of wrought Ti6Al4V without machining. In contrast, L-PBF can have similar fatigue limit as wrought material after either shot peening or centrifugal finishing. The fatigue response is however not only dependent of the surface roughness since the residual stress have a large effect on the fatigue limit. The surface residual stresses are presented in Fig. 2.6-4 and centrifugal finishing and shot peening introduce considerable compressive residual stresses which is beneficial for the fatigue strength. However, the laser shock peening process failed to introduce any large compressive stresses which then is reflected on the fatigue limit in Fig. 2.6-5. Furthermore, one can see that the residual stresses of centrifugal or shot peened E-PBF material are not enough to overcome the drawback caused by the remaining surface valleys and the final fatigue behaviour is determined by the combination of surface roughness, subsurface defects and residual stresses.

The behaviour after post processing was further verified by fatigue tests with variable amplitude loading (Short FALSTAFF spectrum) and the variable amplitude fatigue response was similar to the constant amplitude fatigue behaviour [2].

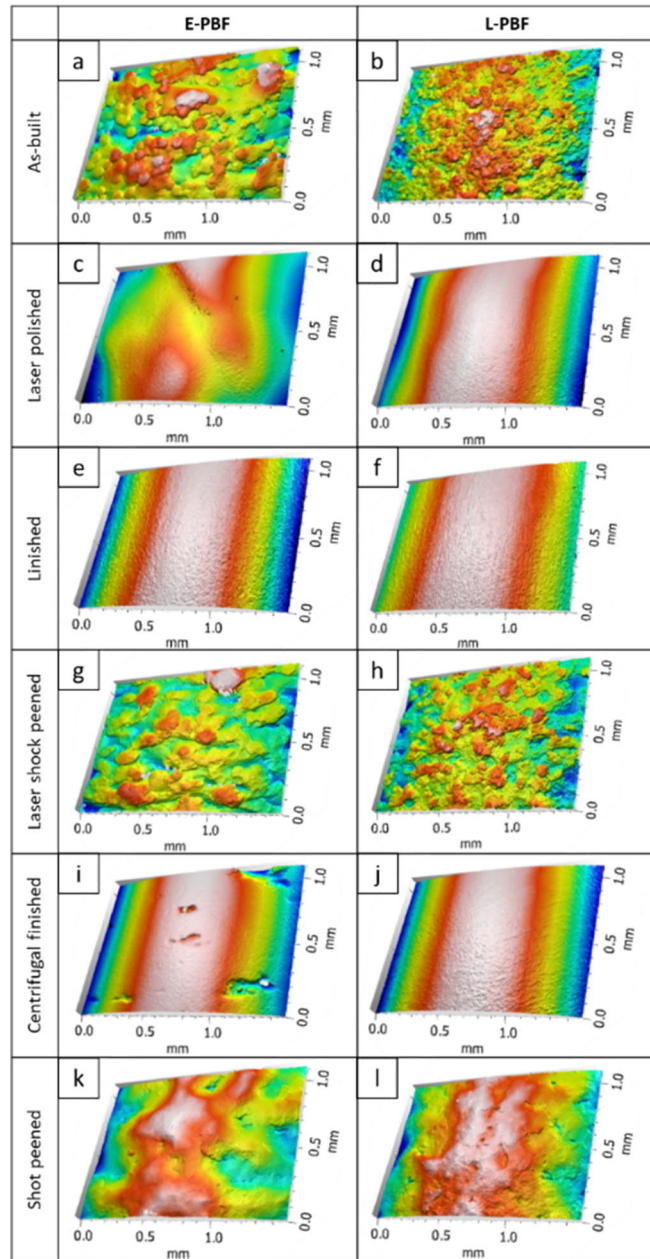


Figure 2.6-3. Surface topography for as-built and post processed surfaces. Image from [1] with courtesy of Elsevier.

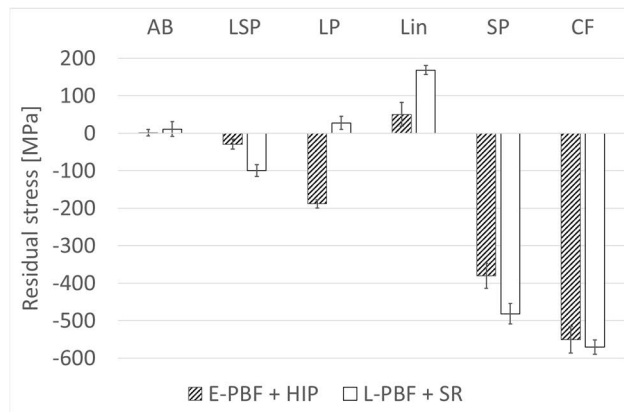


Figure 2.6-4. Surface residual stress measured using X-ray diffraction. AB=as-built, CF=centrifugal finishing, LSP=laser shock peening, SP=shot peening, Lin=linishing, LP=laser polishing. Image from [1] with courtesy of Elsevier.

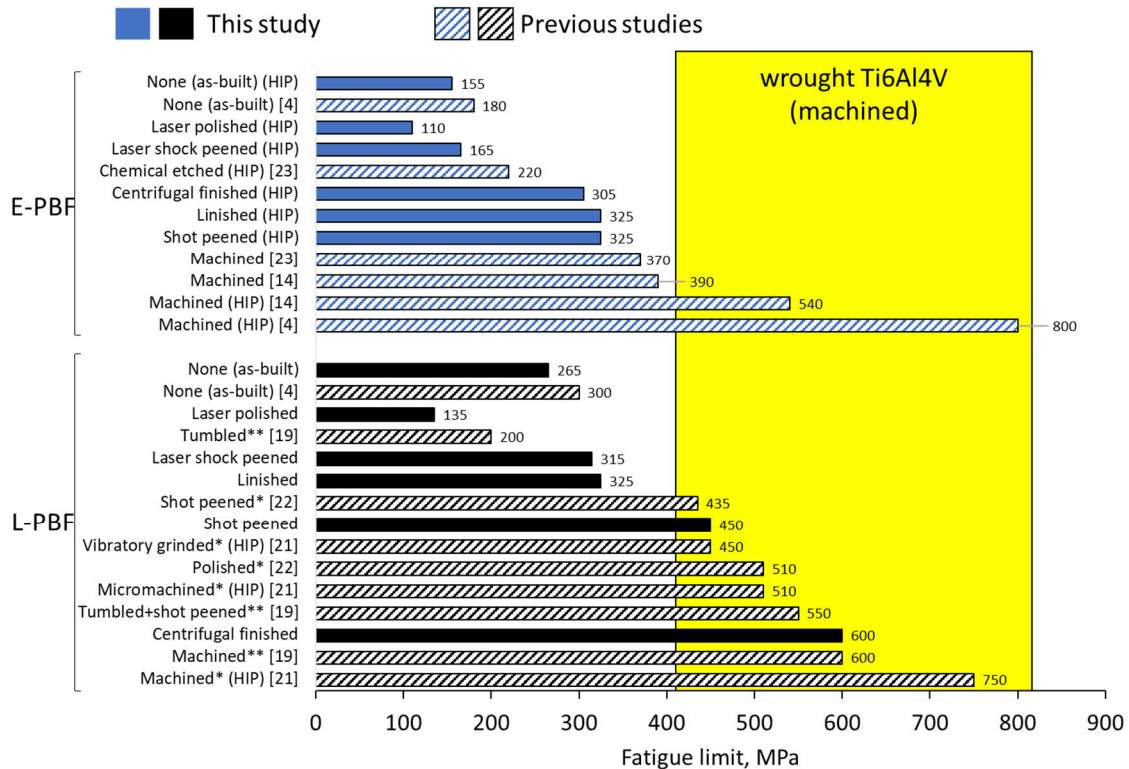


Figure 2.6-5. Fatigue limits for E-PBF and L-PBF Ti6Al4V. Stress ratio $R=0.1$ and specimens loaded in the building direction (Z) unless otherwise stated. * 45° , ** $R=0$. Data references [1,2,11,3–10]. Image from [1] with courtesy of Elsevier.

Conclusions

Additively manufactured Ti6Al4V with as-built surface was subjected to surface post processes in order to improve the fatigue strength:

- Laser powder bed fusion (L-PBF) material could be improved to strength levels comparable to wrought Ti6Al4V by either centrifugal finishing or shot peening.
- The fatigue strength of electron beam powder bed fusion (E-PBF) was improved with more than 100 % by surface post processing but was still inferior to wrought material due to remaining valleys in the surface that could not be removed by the post processing.
- The surface roughness is not a sufficient indicator of the fatigue strength since the final fatigue response is depends on the combination of residual stress, surface roughness and any defects located very close to the surface.

References

- [1] Kahlin M, Ansell H, Basu D, Kerwin A, Newton L, Smith B, et al. Improved fatigue strength of additively manufactured Ti6Al4V by surface post processing. *Int J Fatigue* 2020;134. doi:10.1016/j.ijfatigue.2020.105497.
- [2] Kahlin M, Ansell H, Kerwin A, Smith B, Moverare J. Variable amplitude loading of additively manufactured Ti6Al4V subjected to surface post processes. *Int J Fatigue* 2021;142. doi:10.1016/j.ijfatigue.2020.105945.
- [3] Bagehorn S, Wehr J, Maier HJ. Application of mechanical surface finishing processes for roughness reduction and fatigue improvement of additively manufactured Ti-6Al-4V parts. *Int J Fatigue* 2017;102:135–42. doi:10.1016/j.ijfatigue.2017.05.008.

- [4] Denti L, Bassoli E, Gatto A, Santecchia E, Mengucci P. Fatigue life and microstructure of additive manufactured Ti6Al4V after different finishing processes. *Mater Sci Eng A* 2019;755:1–9. doi:10.1016/j.msea.2019.03.119.
- [5] Wycisk E, Emmelmann C, Siddique S, Walther F. High Cycle Fatigue (HCF) Performance of Ti-6Al-4V Alloy Processed by Selective Laser Melting. *Adv Mater Res* 2013;816–817:134–9. doi:10.4028/www.scientific.net/AMR.816-817.134.
- [6] Persenot T, Buffiere JY, Maire E, Dendievel R, Martin G. Fatigue properties of EBM as-built and chemically etched thin parts. *Procedia Struct Integr* 2017;7:158–65. doi:10.1016/j.prostr.2017.11.073.
- [7] Kahlin M, Ansell H, Moverare JJ. Fatigue behaviour of notched additive manufactured Ti6Al4V with as-built surfaces. *Int J Fatigue* 2017. doi:doi.org/10.1016/j.ijfatigue.2017.04.009.
- [8] Svensson M, Ackelid U, Ab A. Titanium Alloys Manufactured with Electron Beam Melting Mechanical and Chemical Properties. *Med. Device Mater. V Proc. from Mater. Process. Med. Devices Conf. 2009, 2009*, p. p 189-194. doi:10.1007/978-4-431-54237-7.
- [9] Military Handbook. Titanium and titanium alloys. Department of Defense; 1974.
- [10] Morrissey R, Nicholas T. Staircase testing of a titanium alloy in the gigacycle regime. *Int J Fatigue* 2006;28:1577–82. doi:10.1016/j.ijfatigue.2005.10.007.
- [11] Niinomi M, Kuo CK, Ma PX. Mechanical properties of biomedical titanium alloys. *Mater Sci Eng* 1998;A:231–6. doi:10.1016/S0142-9612(00)00201-5.

3 FATIGUE AND DAMAGE TOLERANCE CHARACTERISTICS OF COMPOSITE MATERIAL AND COMPOSITE-ALUMINIUM HYBRID STRUCTURE

3.1 Fatigue testing of hybrid CFRP-aluminium structure at elevated temperature

Zlatan Kapidzic (Saab AB), Amanda Millinger Nylander (Saab AB)

The use of CFRP composite in the airframe structure of Gripen E/F has increased relative to the previous versions of the aircraft. This increase has led to a significant number of continuous CFRP-aluminium interfaces where the materials usually are assembled by bolted joints. Assembling of materials with dissimilar properties, such as CFRP and aluminium, raises several structural integrity related issues:

- Thermally induced loads caused by dissimilar thermal expansion properties of the joined materials.
- Dissimilar mechanical and fatigue properties involve several different damage and failure mechanisms that need to be accounted for in design.
- Dissimilar fatigue scatter [1], which raises questions about the applicability of test factors [2] and test strategies.
- How to implement the Building Block Approach [3] for hybrid interfaces.

Some work related to the above issues has been conducted within GARTEUR project SM/AG-35: Fatigue and Damage Tolerance Assessment of Hybrid Structures. Recently, Saab has initiated a test campaign within IntDemo project [4] to address some of the issues related to the subject of hybrid structure. Some details are outlined below.

Background and goal of the test campaign

When new materials or new structural concepts are introduced the Building Block Approach process is conducted from the bottom up. The coupon level tests are performed first, then element test, then tests of smaller or larger assemblies and finally verifying structural tests. The high level tests are not necessarily run to failure, in which case the critical failure mode is not demonstrated. The idea with the current testing campaign is to first conduct a relatively large hybrid assembly fatigue test to failure at elevated temperature, identify the critical failure modes and then test-study them on coupon level.

Hybrid assembly test (generic wing-box)

The assembly test object is a bolted, generic wing-box structure with aluminium spars, ribs and a splice, covered with 4 CFRP skins, see Fig. 3.1-1. The wing-box also contains:

- Different fastener installation types and fasteners
- Different configurations of ply drop-off regions
- Artificial delaminations (half-circular teflon inserts) in the ply drop-off regions
- Two impact damages in the CFRP skins
- Two main hybrid butt joints and a number of continuous longitudinal joints

The structure is sized for low fatigue margin for four DSL, with respect to the critical parts of the bolted joints based on the available sizing methods. The composite panels and aluminium parts are sized for static loading based on calculated general stress/strain levels.

The wing-box is fatigued in a four-point bending-twisting setup using four load cylinders attached to the box via steel frames, see Fig. 3.1-2. Short FALSTAFF sequence is used. During the cycling the wing-box is placed in an insulated container where hot air is fanned in and the temperature is controlled. The temperature up to 90°C is applied in the test. Around 20 strain gauges are used to continuously monitor the strains at chosen points. Regular ocular and NDT inspections were performed at the joints and defects/damages respectively. An FE-model of the wing box and the loading arrangement is used to study the strains, see example in Fig. 3.1-3.

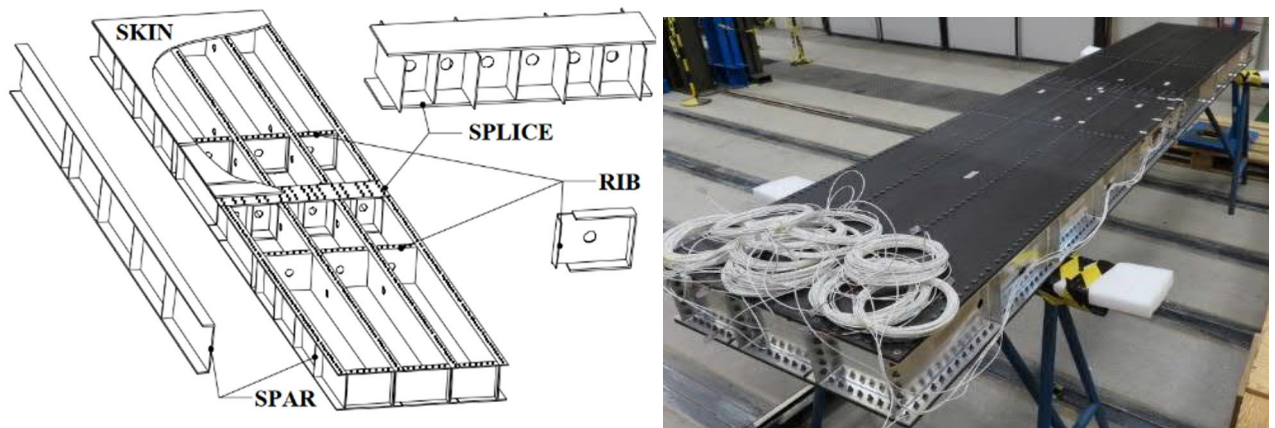


Figure 3.1-1. Wing-box test object.



Figure 3.1-2. Test rig (left) and load introduction (right).

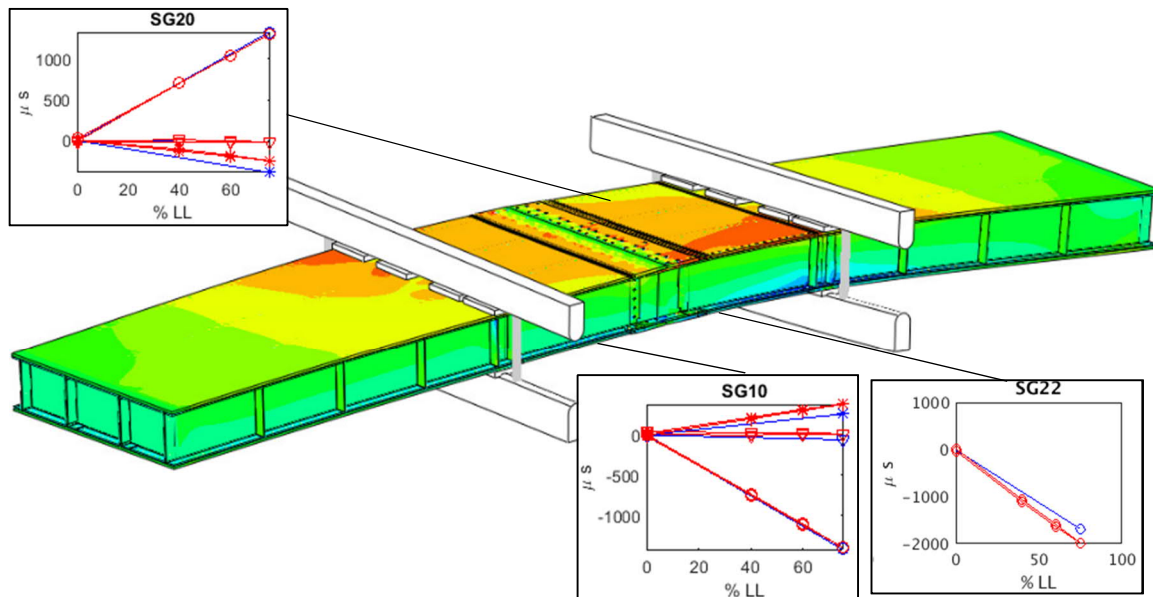


Figure 3.1-3. Strains calculated by FEM (blue) and measured (red).

The test has been run for 4 DSL where after fatigue failure was detected in three bolts in the main splice joint on lower wing side, see Fig. 3.1-4. An irregularity, in form of a slight increase in the strain and displacement measurements at ~ 3.8 DSL indicates the occurrence of the failures. The failed bolts shall be replaced before the test is loaded up to ultimate load and subsequently to static failure. Thereafter, teardown of the test object shall be performed and inspections of all parts, including the defects and impact damages, shall be conducted as well as a great deal of structural and fatigue analyses.



Figure 3.1-4. Three failed bolts in the main joint (left), fatigue crack under bolt the head (middle) and fatigue crack in the bolt thread (right).

Coupon tests

Further testing shall include coupon tests of butt joints. The idea is to study the fatigue life and failure in joint specimens of similar configuration to the joints in the wing-box assembly and variations of it.

Around 150 specimens in 10 different configurations shall be tested in static, CA and VA (Short FALSTAFF) loading at different applied load levels. The baseline specimen configuration has the same materials, dimensions and fasteners as the main splice joint in the wing-box. The other configurations include variations such as: different fastener sizes, plate thicknesses, materials (all aluminium or all CFRP), shims (liquid or sealant) and pretension torque. Lateral support similar to the one shown in Fig. 2.2-2 shall be used to reduce the secondary bending in the specimens. The relative plate displacements shall med measured during the cycling by DIC and extensometers to monitor the joints stiffness.



Figure 3.1.5. Hybrid coupon specimen.

The work is supported by the Sweden's Innovation Agency as grant agreement No. 2020-00187.

References

- [1] Rouchon J. Fatigue and damage tolerance evaluation of structures: The composite material response. In 22th Plantema memorial lecture, 25th ICAF symposium, Rotterdam, 2009.
- [2] Seneviratne WP, and Tomblin JS, "Certification of Composite-Metal Hybrid Structures using Load-Enhancement Factors," FAA Joint Advanced Materials and Structures (JAMS)/Aircraft Airworthiness and Sustainment (AA&S), Baltimore, MD, 2012.
- [3] MIL-HDBK-17-3F. Military handbook, polymer matrix composites. U.S. Department of Defense, 2000.
- [4] IntDemo - Internationellt flygtekniskt demonstratorprogram för ökad konkurrenskraft, miljöanpassning och flygsäkerhet, Diariernr: 2020-00187.

Table 3.4-1. Materials used and its orientation

Laminate ID	Materials used	Orientation
1	50% T80 + 50% UD	$[\left(\frac{0}{90}\right)/45/\left(\frac{0}{90}\right)/-45/\left(\frac{0}{90}\right)]_3s$
2	100% T80	$[\left(\frac{0}{90}\right)/\left(\frac{45}{-45}\right)]_{10}s$
3	100% UD	$[(0/90/45/-45)]_3s$
4	100% T160	$[\left(\frac{0}{90}\right)/\left(\frac{45}{-45}\right)]_5s$
5	50% T160 + 50% UD	$[\left(\frac{0}{90}\right)/45/-45/\left(\frac{0}{90}\right)/45/-45/\left(\frac{0}{90}\right)]_{1,5}s$

Results

Bearing strength

The main aim of the work was to investigate the bearing strength of all the five layups mentioned above. Table 2 shows the values of onset force, onset strength, ultimate bearing force, ultimate bearing strength (UBS) of all the five layups after bearing test. Out of all the layups, 100% UD is kept as the reference and then is compared with each other to identify the best layup. From Table 2, it is seen that 100% T80 has the higher ultimate bearing strength of 1134MPa and highest onset strength of 704 MPa when it is compared with other layups.

Table 3.4-2. Onset force, Onset strength, Ultimate bearing force and Ultimate bearing strength values from the tests

Lam ID	Materials used	Onset force (kN)	Onset strength (MPa)	Ultimate bearing force (kN)	Ultimate bearing strength (MPa)
1	50% T80	13.7	602.6	22.1	1102.9
2	100% T80	10.9	704.0	20.0	1134.1
3	100% UD	8.9	515.0	15.9	1040.0
4	100% T160	11.3	595.4	20.3	1068.7
5	50% T160	9.3	508.4	18.7	909.1

All laminates were designed to have about the same Fibre areal weight as close as possible (with respect to general laminate design rules). But the three preregs used for the 5 layups, were impregnated with different amount of matrix; Fibre volume fraction differed between them, resulting in laminates with some differences in thickness. Also the actual manufactured specimens differed from the theoretical thicknesses, therefor an actual correlation factor to normalize the strength values was obtained using the matrix burn-off method. The results are shown in Table 3.

Table 4.3-3. Theoretical and experimental values of calculated fiber volume fraction.

Materials used	Fiber volume fraction (theoretical)	Fiber volume fraction (experimental)	Factor (experimental)
50% T80	51.6%	53.4%	0.9
100% T80	47.3%	48.9%	0.83
50% T160	51.1%	59%	1
100% T160	54.5%	59.2%	1
100% UD	56.9%	58.8%	1

The Figure 3.2-2 and Figure 3.2-3 show the results of onset strength and ultimate bearing strength respectively of all the five layups obtained after the compensation made due to matrix off burn test. It is clearly seen from the compiled data that the values of onset strength and the ultimate bearing strength of 100% T80, with completely thin plies, is the highest of all tested laminates. Although 100% T160 is made of completely thin plies, the value obtained for onset strength and the ultimate bearing strength is lower than that of 100% T80.

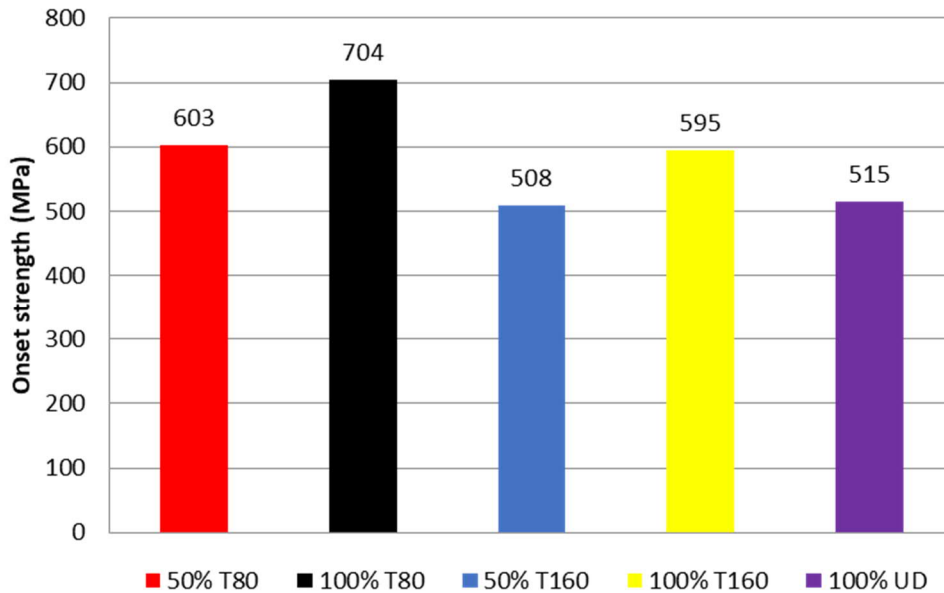


Figure 3.2-2. Onset strength of all layups

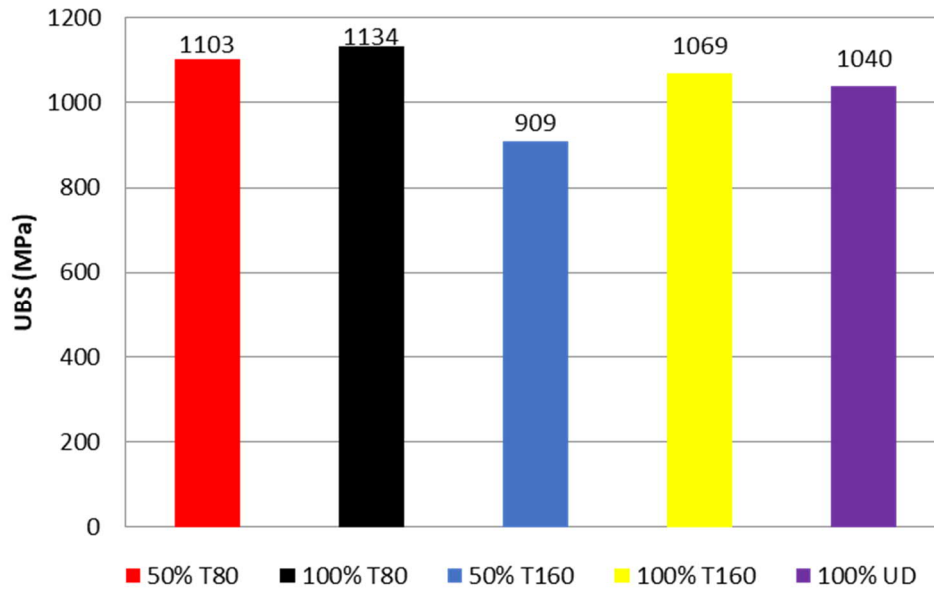


Figure 3.2-3. Ultimate bearing strength of all layups.

Figure 3.2-4 shows the results of the ratio of the onset strength to ultimate bearing strength. It is seen that 100% T80 has the higher ratio i.e, the onset strength to ultimate bearing strength of the layup is 62% of the ultimate strength which is a very good value as the layup can take more load within the elastic limit when compared to the other layups and this is the biggest advantage of using the thin plies. All TeXtreme layups used in this work i.e, 50% T80, 50% 160, 100% T160 fall under the same group as they have the onset strength 55% of its ultimate strength. This value of percentage reduces when the thick plies are added, in case of 100% UD.

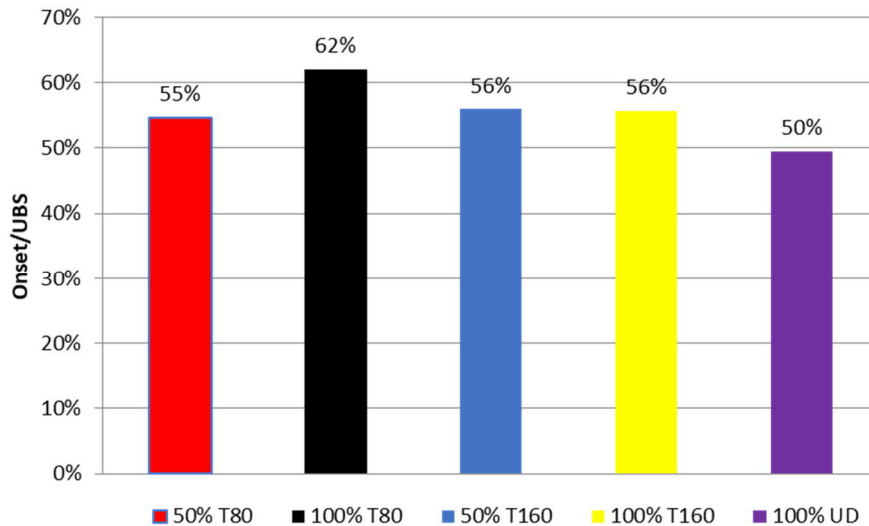


Figure 3.2-4. Ratio of onset strength to ultimate bearing strength for all the layup.

Failure analysis

Bearing Damage

The major type of bearing failure mode witnessed in this work is mainly bearing and net tension failure as shown in Figure 3.2-5. Apart from these two damages, fiber kinking, delamination

and matrix crack are the other types of damages that are further shown in the microscopy analysis.



a) Bearing failure Lam ID 3, 100% UD



b) Net tension failure Lam ID 2, 100% T80

Figure 3.2-5. Bearing failure modes in composite joints after testing.

Microscopy failure analysis

The main objective of this section was to characterize the modes of failure present in the tested specimen.

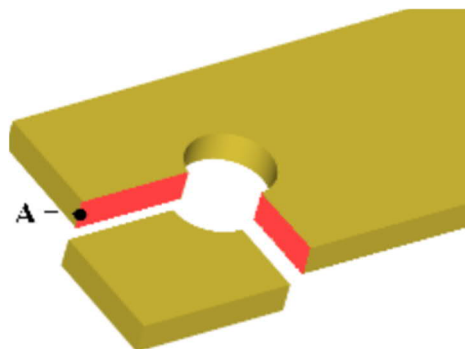


Figure 3.2-6. Area looked at microscope for damage.

All specimens characterized here were not tested until ultimate strength. Figure 3.2-7 shows an example of the bearing stress/strain curve of specimens which were loaded up to 70%, 80% and 100% of ultimate bearing strength.

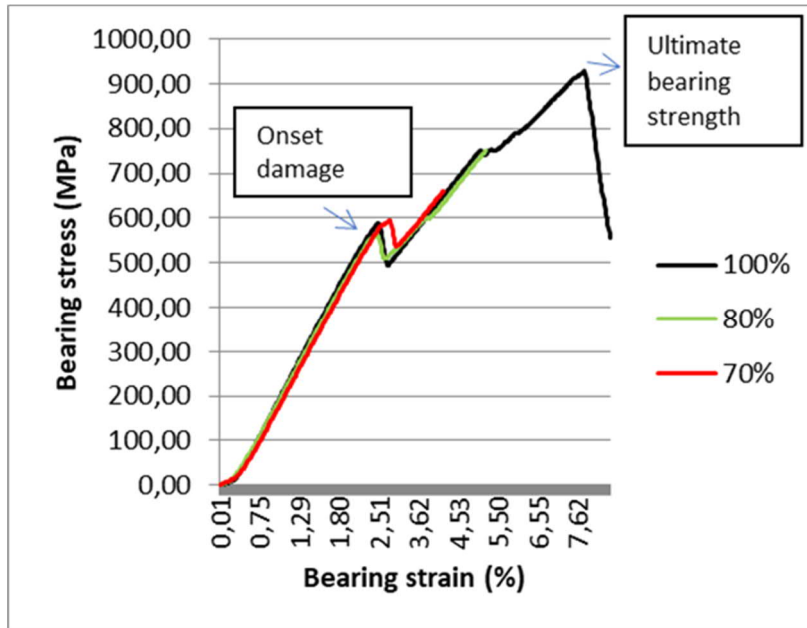


Figure 3.2-7. Bearing stress/strain curve of 100% T80 loaded at 70%, 80% and 100% of its ultimate load.

Point A in the Figure 3.2-6 shows the edge where the specimens were characterized for the damage under the optical microscope. Results are presented in Figures 3.2-8 and Figure 3.2-9.

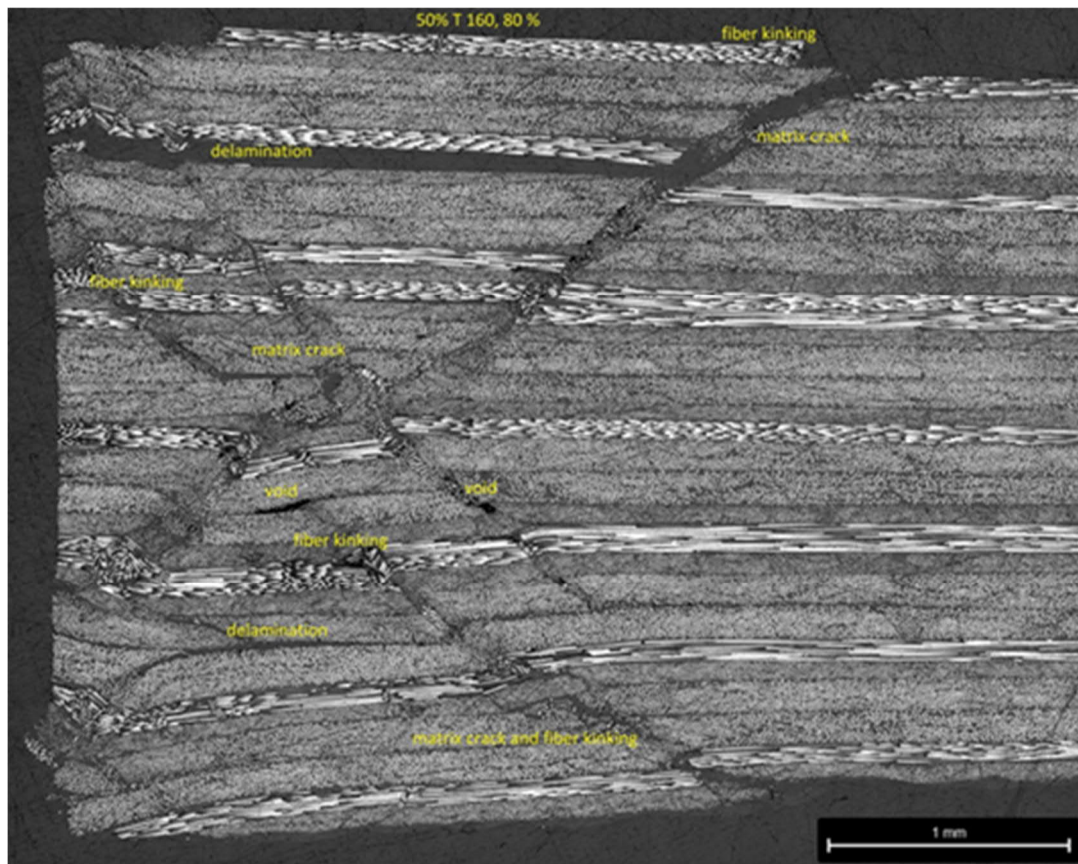


Figure 3.2-8. Fractography of 50% T160 and the damages caused at 80% of its ultimate loading.

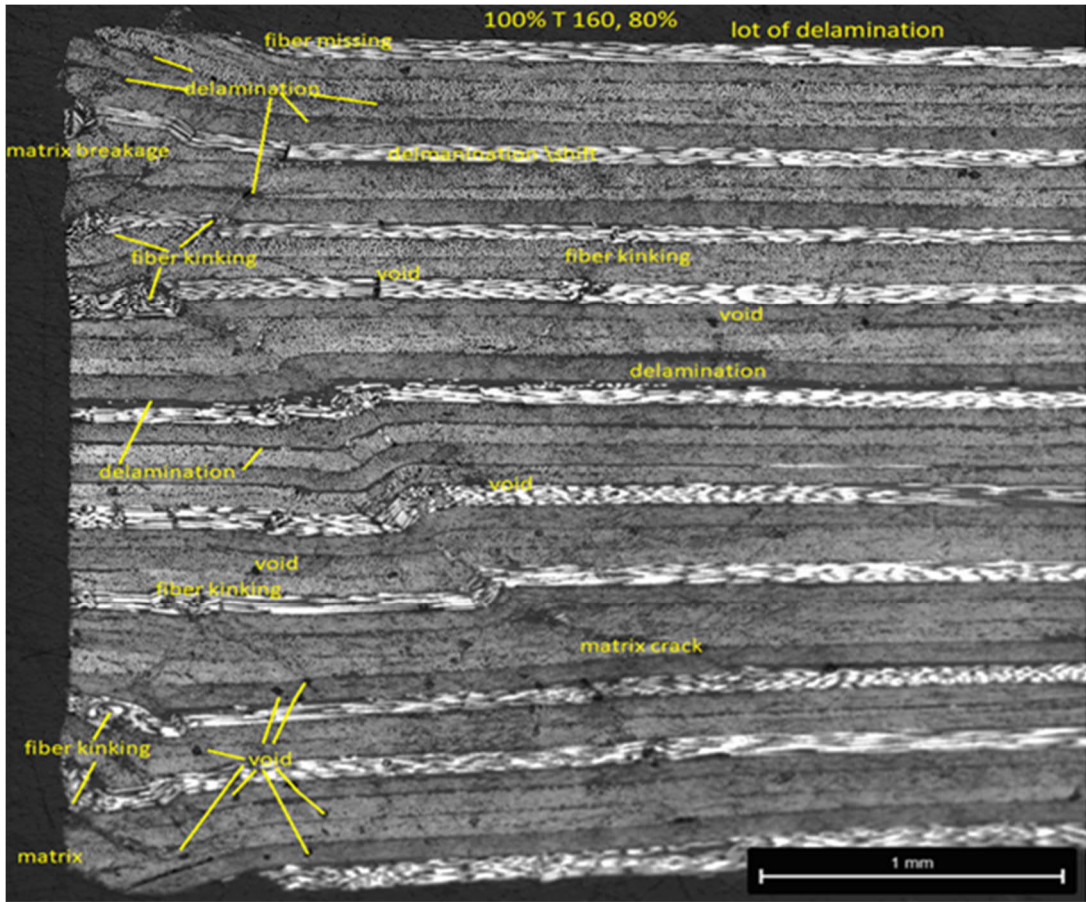


Figure 3.2-9. Fractography of 100% T160 and the damages caused at 80% of its ultimate loading.

All the damages are found but there must be a common basis to compare all the materials as they have nothing in common except for the amount of fibers used. Hence to bring this all together, the microstructure is normalized for the 2 major damages i.e, delamination and fiber kinking. To do this, the microstructure of all the material layup is divided into 7 equal zones which is 0.5 mm apart. And then, the number of fiber kinks in each zone is counted and graph is plotted with the sum of total kinks/ 0° layers versus the equidistant zones as it goes away from the hole.

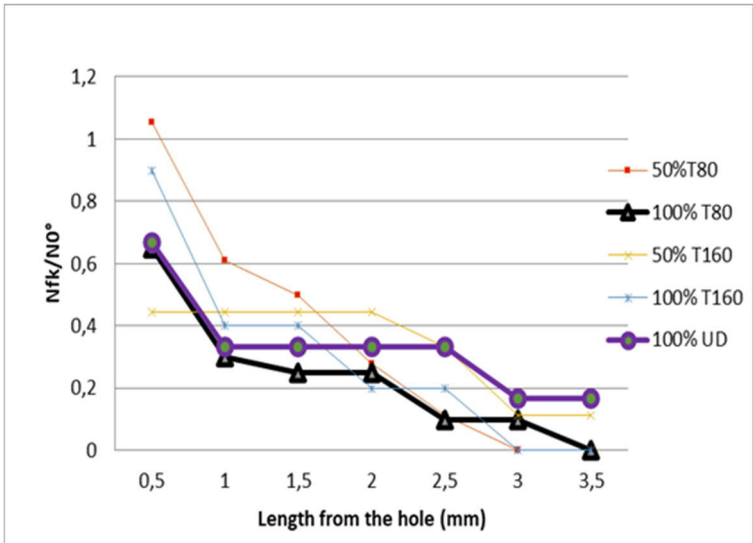


Figure 3.2-10. Normalized results of fiber kinking in all the layups which were loaded up to 70% of its ultimate load.

Figure 3.2-10 shows the results of normalized fiber kinking which were loaded up to 70% of its ultimate load. It is clearly seen in the graph that every layup follows a typical pattern where there is a downfall in the number of kinks present as it goes away from the hole. The TeXtreme material 100% T80 has a smaller number of kinks when compared to other layups. We did not see a huge difference between the specimens loaded up to 70% and 80% of its ultimate load. It also must be noted that in few specimens like 50% T160 in Figure 3.2-8, there are few parts missing in the top and bottom layer which gives a flat line in the curve up to certain distance and this does not mean that 50% T160 is better than 100% T80 which is completely made of thin ply.

4. Conclusion

The effect of using thin plies to increase the bearing strength of composite laminates has been examined. 100% T80 outperformed all layups with highest onset strength of 704 MPa and highest ultimate bearing strength of 1134 MPa when compared to all five layups. Although the manufacturing of thin plies for aerospace applications is expensive, it can be designed in a way such that, there is a transition from thick plies to hybrid thick / thin plies for i.e. areas where there is more stress concentration due to joining using bolts.

3.3 Fatigue after impact of thin ply composites

Zlatan Kapidzic (Saab AB), Mats Bergwall (RISE), Florence Moreau (Oxeon AB)

Thin-ply composites have recently been receiving significant interest in the composite industry. The motivation for this trend toward thinner plies is not only to allow the production of thinner and lighter laminates and structures, but also to provide enhanced strength and damage resistance due to increased laminate design space and positive size effects. By reducing the ply thickness in a multidirectional laminate, the in-situ effect, characterized by an increase in transverse tensile and shear strength of a lamina constrained between two plies with a different fibre orientation, can be observed. Matrix cracking and delamination can therefore be delayed, providing high strength and enhancing fatigue life.

The main objective of this study is to investigate the effect of using thin plies on the fatigue performance of impacted composite laminates by testing.

Test matrix

Three laminate types have been included in the study, see also Table 3.5-1:

- Laminate A is made of conventional UD prepreg used by Saab
- Laminate C is made of conventional UD prepreg made by Oxeon AB
- Laminate B is a hybrid laminate made of same conventional UD prepreg as Laminate B and thin plies made of the same material. Note that the difference between Laminates B and C is only in the arrangement of the material.

	Plies	Material	Layup
Laminate A	UD only	Hexply AS4/8552	[(0/90/45/-45) ₃] _S
Laminate B	UD + Thin-ply	MTC400-UD128T700-12K-34%RW MTC400-Textreme 1001-80gsm 43%RW	[(0/90)/45/(0/90)/-45/(0/90) ₃] _S
Laminate C	UD only	MTC400-UD128T700-12K-34%RW	[(0/90/45/-45) ₃] _S

Table 3.5-1. Studied laminates, (thin plies marked in red), all specimens were ~3 mm thick.

Seven specimens of each laminate were manufactured and six of them were then fatigue tested while one was used to adjust the impact energy in order to obtain appropriate size damage.

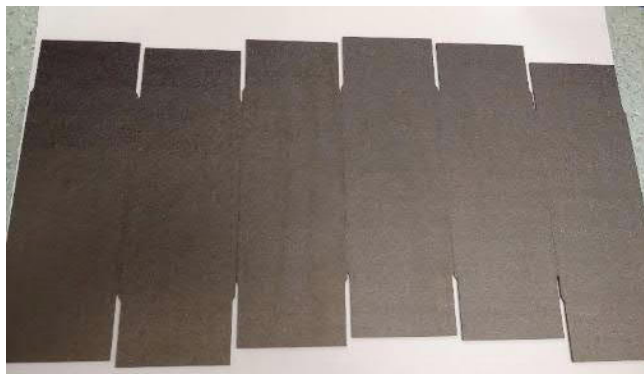


Figure 3.3-1. Specimens, Laminate A.

Test procedure and results

All specimens were impacted by ~11.5 J and dent depths of ~0.5 mm were measured. The impact curves were similar for Laminate B and C but the curves for Laminate A differed, see Fig. 3.3-2. The smaller deflection in Laminate A is probably due to different matrix. NDT C-Scan was used after impact and during the fatigue loading to measure the damaged area in all specimens. Although the impact energies were the same there was difference in the sizes of the damaged area, both between the laminate types and within the same laminate type.

An anti-buckling support device was used to stabilize the specimens and to introduce to load to the specimens. It was designed similar to ASTM D6484/D6484M standard but wider and with some changes to accommodate for NDT measurements, see Fig. 3.3-3.

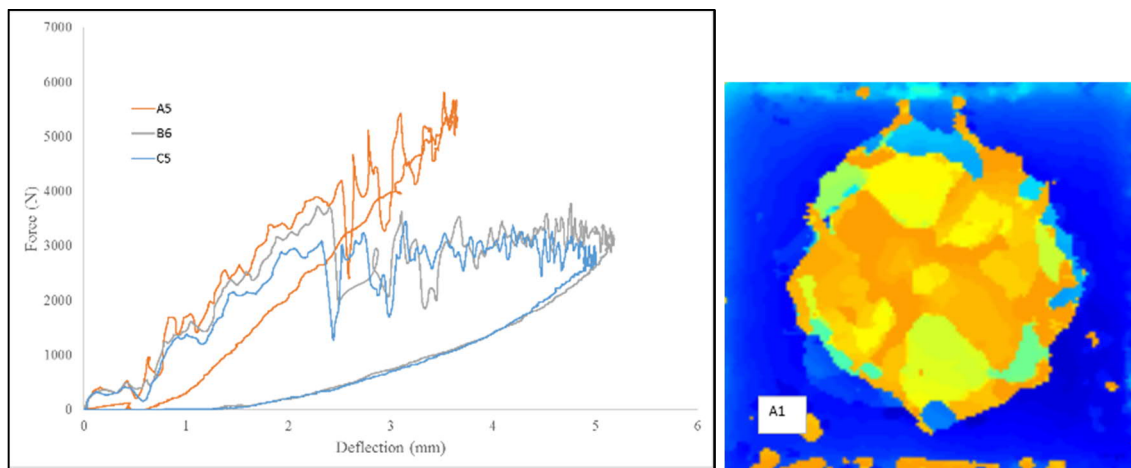


Figure 3.3-2. Typical impact curves and C-Scan of an impact damage.



Figure 3.3-3. Specimen mounted in the support device.

Fully reversed, constant amplitude loading was applied to all specimens until failure or run-out, while different amplitudes were applied in order to obtain the ϵ -N curves, Fig. 3.3-5. Laminate stiffness was measured by DIC virtual extensometers during the cycling and the NDT-measurements were taken frequently to monitor the damage growth, Fig. 3.3-4. The degradation of the stiffness seems to follow a similar pattern for all laminates and can be correlated to the damage growth. Delamination growth initiated shortly before a significant drop in the stiffness was detected.

Laminate A had the highest load capacity but also has the highest stiffness in the pristine condition, which is why the ϵ -N curves for Laminates B and C are higher than A. Although the number of tested samples is too low to draw accurate conclusions the test results indicate that the hybrid Laminate B has better fatigue properties than its conventional counterpart, Laminate C. It is reasonable to assume that a similar increase in fatigue performance would be achieved by adding thin-ply in Laminate A as well.

A hybrid layup, i.e. a mix of thin and thick plies, is more cost effective than a full thin-ply layup, since impact on production still is limited. Therefore the results with the improved fatigue properties are of high interest for the aerospace industry.

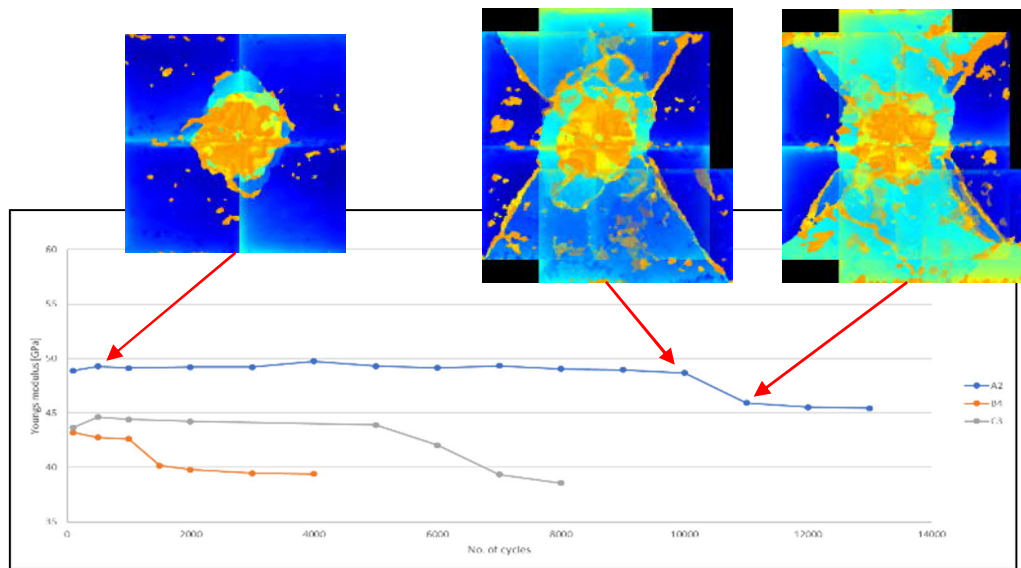


Figure 3.3-4. Measurements of laminate stiffness and damage growth.

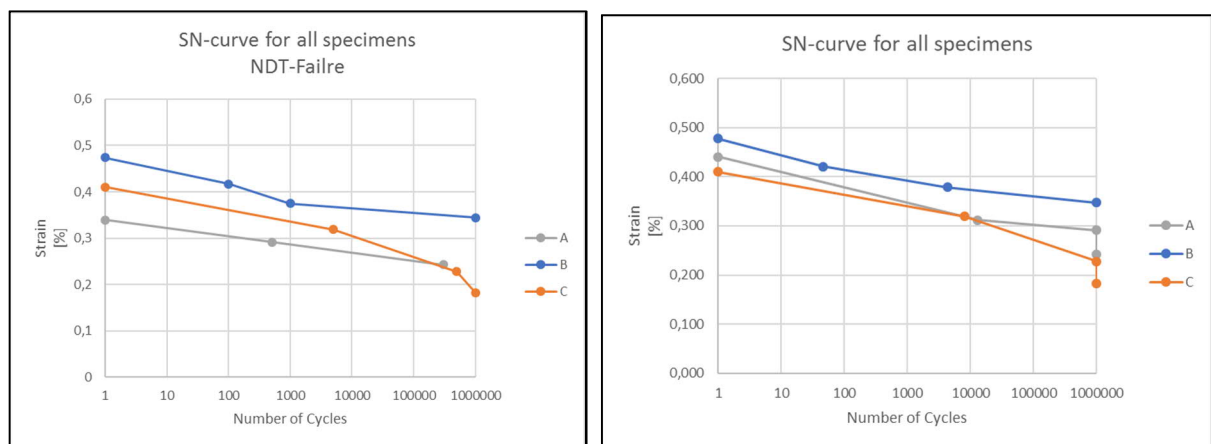


Figure 3.3-5. Fatigue curves, applied strain vs. number of cycles to initiation of damage growth (left) and to failure (right).

This project was funded by Sweden's Innovation Agency as grant agreement No. 2018-04776.

References

- [1] Bergwall M. Fatigue performance of composite laminates after impact. Report Number: CR19-015, 2020.

3.4 Modelling of composite bearing damage

Sergio Costa (RISE)

Introduction

Predictable damage models help designing composite parts more competitively by replacing more expensive tests with cheaper simulation. The present model is based on Continuum Damage Mechanics (CDM), i.e. there is a damage variable accounting for the type and distribution of the damage mechanisms at the ply level. The nonlinear shear behaviour combines damage and friction as first shown to composite materials by [1] and later improved and validated in 45 degrees arrow shape specimen by [2].

Damage modes

During damage growth of composite materials, there are different intraply mechanisms occurring such as fibre kinking and matrix cracking. The fibre compression is modelled simply with a maximum stress bilinear law. However, the possibility for matrix shearing and cracking is accounted at each material point, i.e. an element initially starting to fail by fibre kinking might change to matrix shearing or cracking. Thus, the interaction and competition between damage modes is thus included at the material point. A schematic representation of the matrix compression and shear is shown in Fig. 3.4-1.

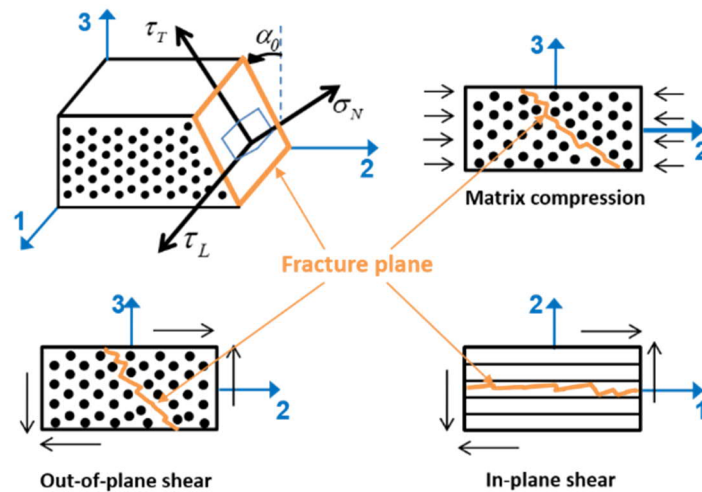


Figure 3.4-1. Intralaminar shear dominated damage modes and their respective fracture plane.

Model simplifications for bearing

The simulation of bearing damage aims at representing the testing made following the ASTM_D5961 standard. However, in order to run the simulation faster the specimen has been simplified. The most important simplification is that only one third of the plied were modelled. This was the obvious choice given the 3s layup. To further speed up the simulation the damage section was reduced to a thinner band, as shown in Fig. 3.4-2. This simplification seems to be acceptable because neither the damage nor the delamination is trying to grow outside this region until late in the loading. However, the drawback of having pure elastic behaviour outside this band is that shear out failure will not be captured by the model. The boundary conditions are representative of the test with the specimen is constrained on one side and a load applied on the axis of the bolt. This bolt is considered rigid.

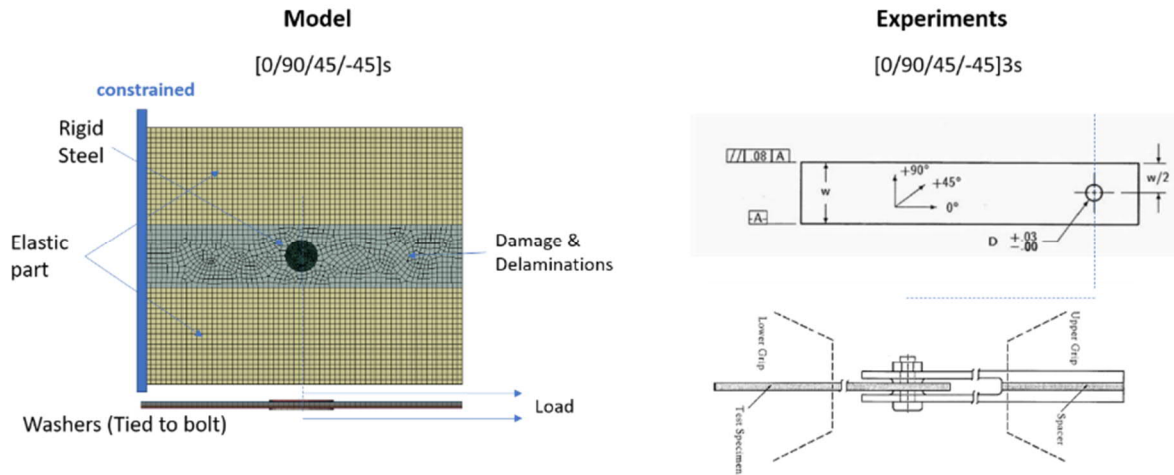


Figure 3.4-2. FE specimen (Model) and schematic drawing of the experiment.

Results: architecture of damage

A good model should be able not only to capture the correct load response but also the mechanisms that occur during that loading. Thus, the model can be considered reliable and able to reduce the reliance on testing for the designing. Therefore, one would like to observe the damage mechanisms happening in every layer, in every interface and at different loading levels. The results are shown in Figs. 3.4-3, 3.4-4 and 3.4-5.

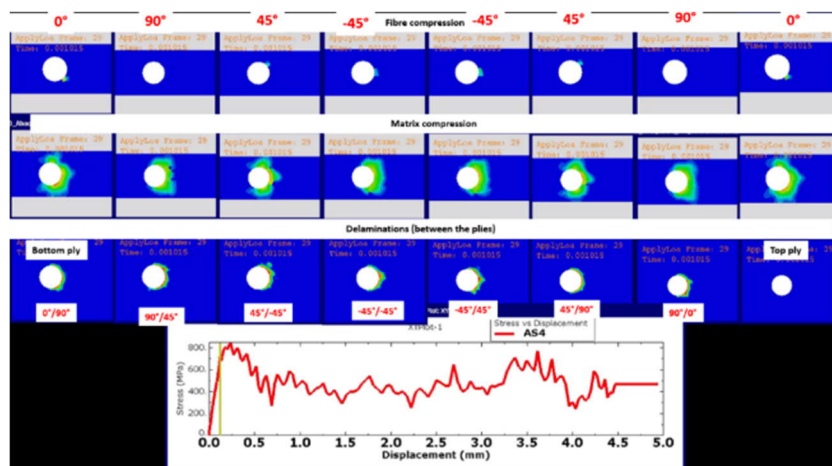


Figure 3.4-3. Damage and delamination before peak load.

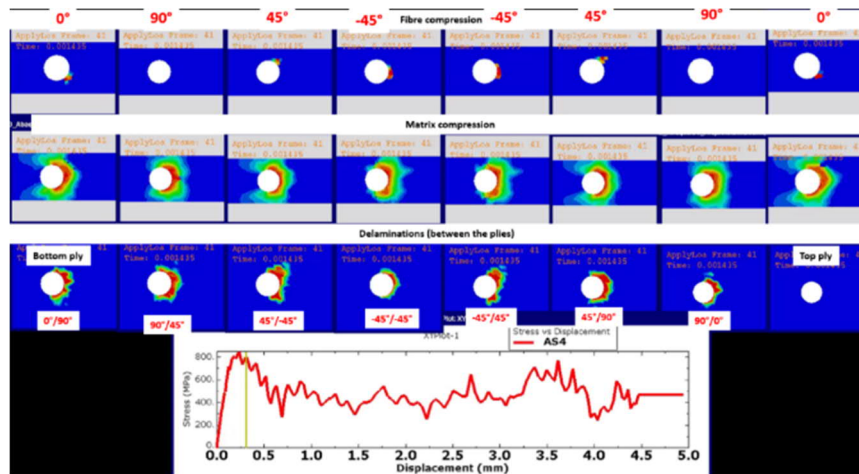


Figure 3.4-4. Damage and delamination after peak load.

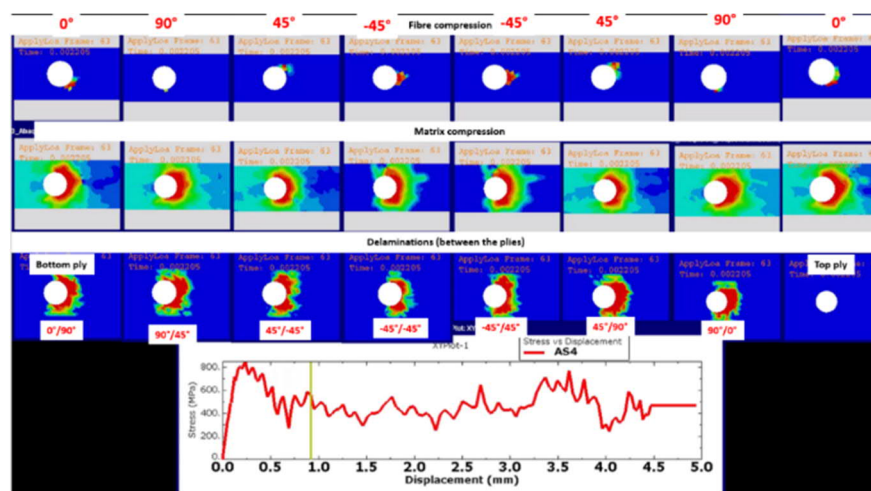


Figure 3.4-5. Damage and delamination at nearly 1 mm intrusion.

Results: load response

Once the architecture of the damage has been considered plausible, the load response is compared with the experiments. The bearing strain vs. bearing stress is shown in Fig. 3.4-6. Overall, the model correlates well. It captures the stiffness and the strength quite well. However, there is a load drop at around 400 MPa that the model is not able to capture. In the experiments this drop is due to fibre kinking. In the model this mode is simplified to a maximum stress criterion and linear degradation which is not representative of the physics involved in fibre kinking. Therefore, as future work, would be interesting to use a physically based fibre kinking model as in [3]. This model considers the shear and transverse stresses as well as the fibre misalignment to determine both the peak load and the response afterwards. The fibres rotate in accordance with the supported by matrix. It would be interesting to see if such a physically based model would be able to capture this drop.

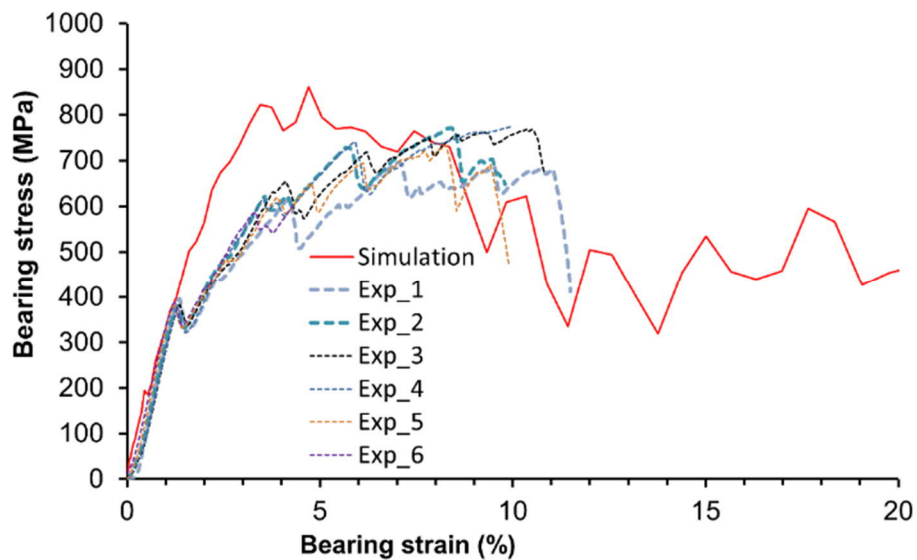


Figure 3.4-6. Experimental vs. simulation: bearing strain vs. bearing stress.

References

- [1] Gutkin R, Pinho ST. Combining damage and friction to model compressive damage growth in fibre-reinforced composites. *J Compos Mater* 2015;49:2483–95. <https://doi.org/10.1177/0021998314549614>.
- [2] Costa S, Bru T, Olsson R, Portugal A. Improvement and validation of a physically based model for the shear and transverse crushing of orthotropic composites. *J Compos Mater* 2018;53(12):1681–1696. <https://doi.org/10.1177/0021998318807964>.
- [3] Costa S, Fagerström M, Olsson R. Development and validation of a finite deformation fibre kinking model for crushing of composites. *Compos Sci Technol* 2020;197. <https://doi.org/10.1016/j.compscitech.2020.108236>.

4 ACKNOWLEDGEMENTS

This editorial work was supported by Saab AB. The editor is also indebted to the following individuals who helped to write this review:

Hans Ansell	Saab AB/LiU
Magnus Kahlin	Saab AB/LiU
Amanda Millinger Nylander	Saab AB
Jan-Erik Lindbäck	Saab AB
Tomi Viitanen	VTT
Risto Laakso	VTT
Keijo Koski	VTT
Mohamed Loukil	RISE SICOMP
Mats Bergwall	RISE SICOMP
Sergio Costa	RISE SICOMP
Stefan Lindström	LiU
Johan Moverare	LiU
Börje Andersson	BARE
Jesse Vickers	Sabreliner Aviation, LLC
James M. Greer, Jr.	CAStLE
Gregory A. Shoales	CAStLE
Florence Moreau	Oxeon AB